

Doctoral Dissertation (Censored)

博士論文(要約)

**A study on the sea surface temperature dependence of
large-scale and mesoscale convective self-aggregations**

(大規模場およびメソスケールにおける対流自己組織化の海面水温依存性に関する研究)

A Dissertation Submitted for the Degree of Doctor of Philosophy

October 2021

令和 3 年 10 月博士(理学)申請

Department of Earth and Planetary Science, Graduate School of Science,

The University of Tokyo

東京大学大学院理学系研究科

地球惑星科学専攻

Shuhei Matsugishi

松岸 修平

Abstract

In Radiative Convective Equilibrium (RCE) experiments that emulate idealized tropical convective activity under uniform boundary conditions, convective activity spontaneously concentrates in a single location without external forces causing a horizontal bias. This phenomenon is called convective self-aggregation (CSA). The mechanism of CSA is related to the radiation, convection, and surface processes. CSA results in drying, increase in radiative cooling, and increase in precipitation. The possible impacts of CSA on the radiative budget and hydrological cycle have been studied in recent years through model intercomparisons such as global, regional, and 2D conceptual models. Its dependence on sea surface temperature (SST) has also been pointed out. It is essential to understand CSA dependence on SST to understand the warming response of convective activity.

The CSA also depends on the computational domain size. Multiple CSA regions may exist if the RCE experiment is performed with a sufficiently large computational domain. The occurrence of regimes in which multiple convective regions are formed suggests a maximum horizontal scale in the self-aggregated convective region. However, the dependence of this horizontal scale on SST is not fully understood. On the other hand, the effects of CSA within an area of about 1000 km square in the real atmosphere have been confirmed based on satellite observations and reanalysis data. Similar changes in the environment during the onset of self-aggregation were observed as in the RCE experiment. However, the dependence of convective aggregation in real atmosphere on SST is poorly understood. In the real atmosphere, focusing on an area of about 1,000 km square, convective activity is affected by large-scale circulations that occur with the SST

gradient and the north-south gradient of solar radiation. It is necessary to account for the influences of large-scale circulation, which differ from the RCE experiment. The SST dependence of CSA in the real atmosphere needs to be examined, considering the effects of large-scale circulation.

In this dissertation, we examine the SST dependence of CSA in two horizontal scales, large-scale and mesoscale. The SST dependence of the maximum horizontal scale of the large-scale aggregated convective region (Chapter 2) was examined as an SST dependence of CSA in a large scale. The SST dependence of mesoscale aggregation (Chapters 3 and 4) was examined as SST dependence of mesoscale in consideration of the influence of the large-scale circulation.

In Chapter 2, the dependence of the CSA on the computational domain size and SST is investigated by conducting RCE experiments using a global model. A single aggregation occurs at small domain sizes, whereas multiple aggregations emerge at sufficiently large domain sizes. The domain-averaged atmospheric temperature and humidity gradually increase with domain size until they reach convergence in cases of multiple aggregations. As domain size increases, surface wind speed increases with the expanded convective region. At the same time, tropospheric temperature increases. Since the moist adiabatic lapse rate caps the lapse rate, there is a limit to the temperature increase, which also places an upper limit on radiative cooling related to the vertical profile of temperature. Surface evaporation must be limited due to the constraint of the energy balance. Consequently, the convective region transitions from single to multiple aggregations to prevent an escalation in surface wind speed. Our results show that the dependence of the horizontal scale of CSA on SST is not monotonic. This dependency is closely related to changes in the structure of the detrainment from the convective region at the melting level, resulting

in enhanced radiative cooling at the top of the boundary layer near the convective region for certain SSTs. This change in the circulation structure leads to increased surface wind speed with increasing domain size. This process affects the non-monotonic dependence of the horizontal scale of CSA on SST.

In Chapter 3, we investigate the dependence of the degree of mesoscale aggregation on SST using observational data. The real atmosphere deviates from the RCE state due to the inhomogeneity of the regional distribution of SSTs. We investigate how convective aggregation is affected by SST and the large-scale circulations that can be regarded as distance to RCE (DRCE). We analyze three indices of convective organization: the simple convective aggregation index (SCAI), the index of the organization (Iorg), and the modified subsidence fraction (SF'). SCAI and Iorg show less aggregation as SST increases, while SF' shows more aggregation as SST increases. However, SF' does not capture important features of aggregation and is considered ineligible as an indicator. Therefore, it is appropriate to use SCAI and Iorg as aggregation indicators. When Iorg and SCAI are used as the quantity of convective aggregation, the higher the SST, the less organized; the higher the DRCE, the more unorganized. In order to clarify the mechanism for the SST dependence, we examined whether the difference in the mean state between the aggregated and disaggregated condition changes in response to SST. The difference in the environment has the same trend as the change in the environment during CSA that occurred in the RCE experiment. There is no clear dependence on SST and DRCE between aggregated and disaggregated mean states. This result indicates that the moist static energy feedback process is unlikely to contribute to the SST dependence of contribute to the SST dependence of mesoscale aggregation in the real atmosphere, contrary to the previous studies using ideal RCE experiments. The increase in convections

associated with higher SST and DRCE was related to disaggregation. However, a tendency for higher SSTs to be less aggregate was also observed for the same number of convections.

In Chapter 4, we conducted numerical experiments to validate the effects of the large-scale circulation discussed in Chapter 3. RCE experiments with an external forcing added to the temperature and water vapor terms were conducted to simulate the equilibrium state with a large-scale upward motion. We observed a trend consistent with the observational study in Chapter 3. As LSF intensifies, convection becomes less aggregate. This trend could be related to an increase in the number of convections. The increase in convections resulted from changes in the environment associated with LSF. There were other factors than the increase in the convective number. Therefore, we conducted a sensitivity experiment in which we weakened the cold pool with convection. It was confirmed that the weakening of cold pools may contribute to less aggregation. Cold pools weaken as SST increases. The cold pools may contribute to less aggregation associated with SST increases.

In this study, we examined the maximum horizontal scale of large-scale convective regions and the degree of aggregation at mesoscale in the real atmosphere as the SST dependence of CSA. We found that changes in circulation structure affect the maximum scale for large-scale aggregation. We pointed out that convection becomes less aggregate as SST increases and the large-scale circulation strengthens, and that cold pools may contribute to the disaggregation. This study partly revealed the SST dependence of CSA at multiple spatial scales. Although the interaction between both spatial scales remains to be clarified, the results of this study provide an advance in understanding how SST affects convective aggregation.

1. General Introduction 1

- 1.1. Convective Self-aggregation in Numerical Simulations under the Radiative Convection Equilibrium..... 2
- 1.2. Convective Aggregation in the Tropical Atmosphere 7
- 1.3. Horizontal Scale of Convective Aggregation 8
- 1.4. Purpose of This Study..... 9

2. Sensitivity of Horizontal Scale of Convective Self-aggregation to Sea Surface Temperature in Radiative Convective Equilibrium Experiments with a Global Nonhydrostatic Model 11

- 2.1. Introduction11
- 2.2. Model and Experimental Design 14
- 2.3. Results 16
 - 2.3.1. Overview of the Equilibrium Solutions of the Simulations 16
 - 2.3.2. Critical Domain Size and Natural Horizontal Scale of Convective Region
21
- 2.4. Why Does Critical Domain Size Exist? 29
 - 2.4.1. Spatial Variance of FMSE Budget..... 29
 - 2.4.2. The Domain Size Dependence of Boundary Layer and Energy Balance.. 32
- 2.5. The SST Dependency of Critical Domain Size 38
- 2.6. Summary and Conclusion..... 44

A. Appendix 49

3. Observational Relationship between the Convective

Aggregation, Sea Surface Temperature, and Large-scale circulation 55

3.1. Introduction	55
3.2. Data and Method	58
3.2.1. Data.....	58
3.2.2. Indices of CSA	58
3.2.3. Distance to Radiative Convective Equilibrium: DRCE	63
3.3. Dependency of CSA on SST and DRCE	64
3.4. Relationship between CSA and large-scale environmental states	70
3.5. Dependency of the number of convection cells on CSA.....	75
3.6. Summary and conclusion	76

4. Convective Aggregation in Radiative Convective Equilibrium with Large-scale Forcing..... 81

4.1. Introduction	81
4.2. Model and Experiment Design	83
4.2.1. Numerical model settings	83
4.2.2. Large-scale forcing based on vertical wind speed.....	84
4.3. Results	87
4.3.1. Dependence of Convective Aggregation on Large-scale Forcing and SST in Larger LSF regime.....	94
4.3.2. Dependence of Convective self-aggregation on SST in smaller LSF regime	103
4.4. Discussion.....	105
4.5. Summary.....	107

5. General Conclusions..... 110

5.1. Summary.....	110
5.2. Concluding discussion.....	113
5.2.1. Relationship among chapters.....	113
5.2.2. Impact of this dissertation	115
5.2.3. Future perspectives	116
Acknowledgments	118
References	119

1. General Introduction

Organized cloud systems are ubiquitous in the tropics and possess a hierarchical structure. In the tropics, convective activity organizes at various spatial scales, from individual cumulus clouds to mesoscale convective systems (Houze, 2004), cloud clusters, super cloud clusters (Mapes & Houze, 1993), the Madden-Julian oscillation (MJO; Madden & Julian, 1972), and the inter-tropical convergence zone (ITCZ). For example, the MJO is a slow eastward-moving cloud system comprising individual cumulus clusters that move westward, forming squall-like structures on scales of several hundred kilometers (Nakazawa, 1988). Organized convective systems affect the radiative budget and the water cycle. Such organized convective activity accounts for half of the tropical precipitation activity (Nesbitt et al., 2001) and affects the radiation budget (Bony et al., 2020). Therefore, understanding the organization of convective activity is crucial in climate science. However, due to their coarse resolution, current climate models cannot explicitly represent the organization of these convective systems. Climate research using a global cloud-resolving model that explicitly resolves the organized cloud systems is desired (Stevens et al., 2019; Satoh et al., 2019).

The organization of convective activity in the real atmosphere is strongly influenced by various horizontally non-uniform conditions, such as the Earth's rotation, sea surface temperature (SST) gradients, and land-sea contrasts. For example, the power spectral density of convective activity assumes the structure of an equatorial wave (Takayabu, 1994). In the tropics, many studies have highlighted the correlation between SST and convective activity (Graham and Barnett 1987; Zhang 1993). Furthermore, the diurnal cycle of precipitation varies between land and ocean. Over the land, precipitation peaks

in the early evening, while over the ocean, it peaks in the early morning. As a result, convection is biased towards land during the day and the ocean at night. In addition, it is observed that convective clouds developing over an island during the daytime propagate over the open ocean from evening to night in the maritime continent (e.g., Mori et al. 2004). Hence, spatially non-uniform external factors, other than convection itself, play a role in the spatially organized structure of convective activity.

Interestingly, in ideal experiments such as the radiative-convective equilibrium (RCE) experiments, convective activity spontaneously organizes into a single cluster without inhomogeneous external forcing or rotation. This phenomenon is widely referred to as convective self-aggregation (CSA; Bretherton et al., 2005). Understanding CSA may lead to an intrinsic understanding of the convective activity. This study will focus on the spontaneous organization of convective activity without spatially non-uniform external forcings, examining the convective organization caused by various factors. We focus on the SST dependence of the maximum horizontal scale of CSA and the mesoscale convective aggregation observed from satellite data.

This chapter consists of three sections: Section 1.1 reviews the basic understanding of CSA in RCE experiments. In section 1.2, The horizontal scale of CSA is introduced in section 1.3. Finally, the motivation for this thesis is presented in section 1.4.

1.1. Convective Self-aggregation in Numerical Simulations under the Radiative Convection Equilibrium

The RCE is considered a statistical equilibrium state where radiative cooling, surface heat transport, and circulation due to convection are balanced. The RCE is widely applied as a first approximation of Earth's climates and is often the initial step in climate research.

Historically, RCE experiments originated with the one-dimensional model of Manabe and Stricker (1964). However, this one-dimensional model required parameterization of the moist convection, leaving no room to discuss spatial aggregation of convection. In the tropics, where convective activity is more dominant than in mid-latitudes, the RCE simulation is widely recognized as the primary approximation for the tropical atmosphere. Therefore, many studies have been made to understand convective activity in the tropical atmosphere by conducting ideal experiments using the radiative-convective equilibrium system. One of the pioneers was Nakajima and Matsuno (1988), who conducted an RCE experiment with a model that explicitly resolved convective clouds in two-dimensional x-z planes. Their experiment showed that convective activity was typically concentrated at one location with a wavenumber-one structure. Subsequent studies (e.g., Held et al., 1993; Sui et al., 1994; Grabowski et al., 1996) using two-dimensional numerical models have shown similar results of convective aggregation in one location. On the other hand, in the initial study of the 3-D cloud-resolving model, such an organizational behavior was not simulated, and scattered convections were simulated (e.g., Islam et al., 1993). In retrospect, this was likely due to the small domain size and short integration time.

With advancements in computational power, it is now feasible to conduct RCE experiments in a three-dimensional cloud-resolving model (CRM) over an extended period (more than 30 days) and larger domain sizes (more than 200 km square) (e.g., Tompkins & Craig, 1998). The RCE experiment with a regional CRM typically follows configuration: the lateral boundary is assumed to be a periodic boundary condition, and the lower boundary condition is considered a uniform constant temperature with sea surface conditions. Shortwave radiation is considered uniformly constant, and there is no diurnal cycle. The integration time generally ranges from 50 to 100 days. The initial

condition is a horizontally uniform vertical temperature and water vapor profile with random small initial noises. For the vertical profile, we use either the typical profile of tropical atmospheric observations or the horizontal-mean profile of the spun-up under a similar configuration with less than 100 km square or a single-column model.

In such RCE experiments, there is no external forcing leading to horizontal biases, and boundary conditions remain horizontally uniform. However, the convective activity spontaneously shifts, becoming biased towards a specific location in the computational domain. The domain is divided into two regions: a moist region with active convection and a dry region with suppressed convection. This phenomenon is widely referred to as convective self-aggregation (CSA) by Bretherton et al. (2005). The typical duration for transitioning from a quasi-uniform initial state with random perturbations to CSA ranges between 15-100 days (Wing et al., 2017). When CSA occurs, the mean state of the simulation becomes dry, increasing radiative cooling and precipitation while decreasing cloud cover (e.g., Bretherton et al., 2005). Enhanced extreme precipitation has also been noted (Bao et al., 2017; Bao & Sherwood, 2019). The onset of CSA depends not only on the physical processes of the numerical model but also on the resolution and domain size of the RCE experiment (Muller & Held, 2012; Yanase et al., 2020). These studies indicate that the CSA occurs more frequently with a coarser horizontal resolution and larger domain sizes.

CSA has been studied not only in regional cloud-resolving models but also in global climate models as well. In the climate model, as in the regional model, the lower boundary is assumed to be a uniform constant sea surface with a fixed temperature. The shortwave radiation is given a globally constant value, and the model domain shape is a sphere without rotation. Unlike many regional CRM simulations, multiple convective regions

are often formed in climate models (e.g., Bony et al., 2016; Wing et al., 2020). Convective parameterizations strongly affect CSA (Becker et al., 2017).

Several fundamental mechanisms have been proposed to explain the occurrence and persistence of CSA. Viewing CSA as amplifying the column-integrated moist static energy (MSE) variance, the feedback processes related to the horizontal variance of MSE have been proposed as a key process of development of CSA (Wing & Emanuel, 2014). Radiative feedback, mainly from longwave radiation, is essential in CSA. The radiative process decreases MSE in the dry region and increases MSE in the moist region, strengthening the MSE gradient. The radiative cooling drives shallow circulation between the dry and moist regions, transporting MSE upgradient and contributing to the generation and maintenance of CSA (Bretherton et al., 2005; Muller & Held, 2012; Wing and Emanuel, 2014). Feedback linked to wind speed anomalies relates to surface fluxes and convection, commonly called WISHE. Within the MSE variance equation, the radiative feedback and surface feedback are observed to be dominant for CSA.

Other studies delve into alternate processes from the MSE variance equation when examining CSA's development. Tompkins and Semie (2017) show that the larger the entrainment associated with convection, the more likely CSA will occur. The cold pools inhibit organization, as indicated by sensitivity experiments that damped cold pools by reduced rain evaporation (Jeevanjee & Romps, 2013). The virtual effect, deriving from water vapor lightness compared to air, has been proposed as a mechanism that creates pressure gradients in the boundary layer and leads to the onset of CSA (Yang, 2018). CSA is a phenomenon in which various mechanisms related to convective activity, such as radiation, surface flux, entrainment, and water vapor itself, are combined to enhance and maintain the contrast between the dry and moist regions.

It has been pointed out that CSA may be dependent on SST. Wing and Emanuel (2014) reported that higher SSTs are more likely to lead to CSA because the longwave radiation feedback in the dry region becomes stronger as SST increases. However, CSA occurs even at low SSTs (e.g., Abbott, 2014; Holloway & Woolnough, 2016). Climate model studies have also pointed out the possibility that enhanced CSA occurs with warming from reduced upper cloud cover resulting from reduced divergent flows associated with increased stability (Stability Iris feedback; Bony et al., 2016). The significant differences between aggregation and scatter states can affect climate sensitivity depending on how the degree of aggregation changes with warming (Becker & Wing, 2020).

Some studies have focused on SST dependence concerning the mechanisms that initiate and maintain CSA. Coppin and Bony (2015) pointed out that the dominant mechanism during the onset of organization varies with SST based on the analysis of the MSE variance equation. They argue that at low SSTs, radiative cooling due to cloud-radiation interactions in the lower clouds enhances the shallow circulation. In contrast, at high SSTs, latent heat flux feedback enhances aggregation. However, this mechanism at the onset of CSA is model-dependent and is reversed in other models (Becker et al., 2017).

Finally, we describe the methods of CSA quantification in previous studies. CSA itself is found in the variance of column water vapor (CWV) or horizontal distribution of CWV. On the other hand, several indices have been proposed to quantify the strength of the aggregation. A typical example is an index based on CWV or column relative humidity. It is quantified by the percentage of domain size in the dry region (Coppin & Bony, 2015). This is because dry regions are downwelling, and moist regions are upwelling when spatial-temporal averages are taken to some extent. Another indicator that is often used in model studies to calculate convective activity is based on its geometric configuration.

A typical one used in model studies is the index of the organization (Iorg) proposed by Tompkins and Semie (2017). Geometric indices are often used to quantify CSA in satellite observations and will be introduced in the subsequent section. Various indices of the degree of the organization are proposed, and we need to use them carefully because they differ in what aspects of the organization they focus on (Cronin & Wing, 2017; Wing et al., 2020).

1.2. Convective Aggregation in the Tropical Atmosphere

Some studies have investigated processes related to modeled CSA in real tropical atmospheres. To consider the correspondence with the ideal experiment, they chose sizeable tropical latitude-longitude boxes (10x10 degrees; Tobin et al., 2012), which are equivalent to the domain size of CRM, or small tropical latitude-longitude boxes (3x3 degrees; Tobin et al., 2013) as the grid-scale of the climate model. Within these boxes, satellite observation data was used to define the degree of convective organization. For example, Tobin et al. (2012) defined the simple convective aggregation index (SCAI) based on the convective cluster number and inter-cluster distance. A more aggregated state was found to be drier and increased radiative cooling and precipitation (Tobin et al., 2012, 2013). However, compared to the ideal RCE experiments, the change in the environmental field to the degree of aggregation was small. Stein et al. (2017) also noted a decrease in upper clouds with aggregation. Semie and Bony (2020) suggest that organizations may impact extreme precipitation.

The SST dependence of the degree of organization is contrary to the hypothesis that it becomes more robust with SST elevation, as pointed out in the ideal RCE experiments. Using three types of organization indices, Xu et al. (2019) pointed out that there is no

tendency for the degree of organization to increase with SST elevation. Noda et al. (2019) also suggest that in a high-resolution cloud system resolution model performed with AMIP types, cloud organizations may weaken with warming in a warming experiment.

The effects of CSA have been investigated on scales larger than 10 degrees square. Capturing large horizontal scale aggregation may offer better correspondence with the RCE experiment because a domain with a spatial scale of 5000 x 5000 km² can be considered an RCE state using satellite observation and reanalysis data (Jakob et al., 2019). Hohenegger and Jakob (2020) showed that the more aggregated Atlantic ITCZs are associated with a moister ITCZ region and drier subtropics. Popp and Bony (2019) pointed out that the Hadley circulation expands in the meridional direction when the convection along the equator is more aggregated in the zonal direction. Bony et al. (2020) discussed the relationship between spatial organization and the global radiative budget. On such a large spatial scale, the effect of the SST gradient also becomes significant, contrasting the uniform SST RCE experiment previously mentioned. Therefore, the effects of SST gradients on the CSA have also been investigated using RCE experiments with SST gradients (e.g., Sebastian & Hohenegger, 2020).

1.3. Horizontal Scale of Convective Aggregation

Next, we will examine the horizontal scale of CSA. In the real atmosphere, convective activity has a hierarchical organizational structure. The relationship between the organization and the environmental field has been pointed out at various spatial scales. Therefore, it is essential to consider the horizontal scale of CSA in the ideal experiment. Within such experiments, the computational domain is the primary constraint on the horizontal scale. Studies of CSA in regional scale CRMs have been conducted for a

domain area of $O(1000^2 \text{ km}^2)$ (e.g., Bretherton et al., 2005; Wing & Emanuel, 2014; Holloway & Woolnough, 2016). In contrast, CSA studies in climate models have been conducted over a global-scale domain size ($5.1 \times 10^8 \text{ km}^2$). The size of the active convective region in the two models differs by a factor of 10, and multiple convection basins are formed in the climate model. In the regional scale model, it is known that as the computational domain size increases, it transitions to an area with multiple convective regions (Arnold & Putman, 2018; Patritio & Randall, 2018). Therefore, there is a maximum scale for self-aggregated convection regions. Its maximum spatial scale is about 4000 km (Arnold & Putman, 2018). This scale is larger than the spatial scale $O(1000^2 \text{ km}^2)$ used in previous CRM studies. As for the spatial scale of the active convection region, studies have been conducted in the quasi-quadratic channel regime (e.g., Wing & Cronin, 2016), with SST dependence decreasing up to 290-310 K and showing an increasing trend after that (Yang, 2018). However, Tompkins (2000) has shown that the onset of convection differs between 3D models and 2D regions in RCE experiments, and thus, it is unclear whether this relationship holds for 3D models.

1.4. Purpose of This Study

It has been confirmed in various ideal experiments that convective activity spontaneously concentrates and organizes itself, and the effects of organization have been detected in the real atmosphere. In the context of climate sensitivity, it is essential to understand the SST dependence of CSA. Traditionally, the focus has been on whether CSA occurs in narrow-domain simulation. However, it has been suggested that CSA always occurs in sufficiently large domain sizes and has a maximum scale in the convective region. The dependence of the horizontal scale of this convective region on

SST has not been sufficiently investigated. In addition, convective aggregation in the real atmosphere often considers the SST dependence of the 1000 km square scale mesoscale, where the heterogeneity of the lower boundary conditions is relatively small. RCE state is not always established in a real atmosphere at such a horizontal scale. It is necessary to consider the effect of large-scale upwelling.

In this study, we aim to clarify the SST dependence of organized convection in the context of CSA observed in RCE experiments. We reveal the maximum scale of the active convective region in the RCE experiment and its SST dependence. For mesoscale aggregation, we focus on the SST dependence of the degree of mesoscale organization and its relation to large-scale forcing. The former will be examined using a large-domain RCE experiment. The latter part is examined using reanalysis data and satellite observations. In addition, RCE experiments with large-scale forcing will be used to follow up to investigate processes suggested by the observational study.

This thesis is organized as follows: Chapter 2 examines the SST dependence of the spatial scale of large-scale correspondence self-organization. Chapter 3 presents the results of investigating the SST dependence of mesoscale spatial aggregation in the real atmosphere using observational data. We also investigated how large-scale forcing affects mesoscale spatial aggregation. In Chapter 4, we present the results of an RCE experiment with uniform horizontal large-scale forcing that mimics conditions corresponding to the real atmosphere. In Chapter 5, general conclusions and future prospects are presented.

2. Sensitivity of Horizontal Scale of Convective Self-aggregation to Sea Surface Temperature in Radiative Convective Equilibrium Experiments with a Global Nonhydrostatic Model

The contents of this chapter have already been published as follows:

Matsugishi, S., & Satoh, M. (2022). Sensitivity of the Horizontal Scale of Convective Self-Aggregation to Sea Surface Temperature in Radiative Convective Equilibrium Experiments Using a Global Nonhydrostatic Model. *Journal of Advances in Modeling Earth Systems*, 14(5), e2021MS002636. <https://doi.org/10.1029/2021MS002636>

2.1. Introduction

Contrary to earlier studies using RCE experiments with limited domain size, recent studies have shown that CSA forms multiple regions in experiments using broader domains. This domain size dependency is also related to the applicability of RCE experiments to the natural atmosphere. Jakob et al. (2019) argued that a domain with a spatial scale of 5000 x 5000 km² could be considered an RCE state using satellite observation and reanalysis data. Therefore, RCE simulations must be conducted with a sufficiently large domain size, with a horizontal scale greater than 5000 km, to avoid the artificial effect of domain size. For example, it has been suggested that the equilibrium state changes with domain size; domain-averaged temperature and moisture become warmer and more humid, respectively (Arnold & Putman, 2018). This horizontal scale of 5000 km is almost comparable with the length (6000 km) of an elongated channel geometry proposed by RCEMIP (Wing et al., 2018). Three-dimensional RCE

experiments with horizontal scales larger than 5000 km have only recently been available, as described below. A “natural” scale of CSA can be defined as the horizontal scale of the convective region in a sufficiently broad domain in which multiple convective regions co-exist. This scale can also be obtained by varying the domain size in RCE simulations. In smaller domains, such as a square domain with a side measuring 100 km (a small domain in RCEMIP; Wing et al., 2018), CSA does not generally emerge. A single cluster is formed if the domain size exceeds than 200 km (Muller & Held, 2012). Multiple convective clusters are formed as the domain size increases to more than 5000 km (Arnold & Putman, 2018). Patrizio and Randall (2019) referred to this domain size as the critical domain size, such that domains below this threshold allow the formation of only a single cluster. Multiple clusters are accommodated if a domain is larger than the critical domain size. In RCE experiments with long channel-shaped domains, multiple convective clusters form along the length of the channel, with a quasi-uniform banded structure across the short width of the channel (Wing et al., 2020).

Another type of RCE experiment considers the global spherical domain using global climate models or global cloud system-resolving models (e.g., Arnold & Randall, 2015; Bony et al., 2016; Ohno & Satoh, 2018; Satoh et al., 2016). The convective region can take various shapes, including planetary-scale banded (e.g., Silvers et al., 2016; Patrizio & Randall, 2019; Reed et al., 2015) or circular (Ohno & Satoh, 2018). CSA is achieved with a natural horizontal scale if the domain is larger than the critical domain size. The critical domain size is around 5000 km for a square regional model with a cumulus convective parameterization (Arnold & Putman, 2018) and cloud-resolving models (Patrizio & Randall, 2019).

RCE experiments are used to test the responses of equilibrium states to underlying SST changes to understand changes in clouds and convective activities associated with global warming. This SST dependency is linked to changes in the CSA regime and the natural horizontal scale of CSA because the equilibrium states are greatly affected by the CSA regime. The dependence of CSA on SST in an experiment with a small domain is misleading because the CSA regime may differ from that in a sufficiently large domain size. According to RCEMIP (Wing et al., 2020), the dependence of CSA spatial scale on SST diverges; it tends to decrease with increasing SST in some channel-domain CRM simulations but increases in global-scale models. Therefore, there is still much uncertainty in the dependence of the CSA horizontal scale on SST.

Several studies have pointed out the importance of boundary-layer processes for the dependence of the CSA horizontal scale on SST. Wing and Cronin (2016) argued that the remoistening time scale of the boundary layer determined the horizontal scales of CSA. Meanwhile, Yang (2018) proposed that boundary layer height and buoyancy primarily associated with the virtual temperature effect determine the horizontal scale of CSA. These studies were based on RCE experiments using domains with a long channel configuration. The wavenumber of the water vapor field along the long axis of the domain was defined as a measure of the horizontal scale of CSA. The horizontal scale decreases as SST becomes warmer across a range of SSTs (290–310 K; Wing & Cronin, 2016; Yang, 2018), while it increases at higher SSTs (310–325 K; Yang, 2018). These studies showed that the boundary layer height decreased, and buoyancy between moist and dry regions increased with increasing SST. Other studies have shown that the pressure gradient increases and the lower-level wind speeds increase with increasing domain size in simulations with a square domain (Arnold & Putman, 2018; Patrizio & Randall, 2019).

The dependence of the horizontal scale of CSA on SST has been studied only in long channel domains, not in a global spherical domain.

In this study, we use a global spherical field to investigate the horizontal scale of CSA and its dependency on SST. We use a global nonhydrostatic model with an explicit cloud microphysics scheme and without a convective parameterization scheme to investigate this dependency for domain sizes in the range between $R/16$ and $R/1$, where R is the Earth's radius. The motivation behind using the realistic size of Earth is to connect the results of the idealized RCE simulations to the natural atmosphere. A comparison by Satoh et al. (2016) between the RCE experiment and an aqua-planet experiment suggested that the horizontal scale of CSA may correspond to the natural scale of the convective cluster along the equator of the aqua-planet experiment, which implies that the RCE results are applicable to the natural atmosphere.

The thesis is organized as follows. In section 2.2, we describe the numerical model and experimental design. Section 2.3 presents the simulation results and the dependence of domain size on specific SST and evaluates the critical domain size and convective region. Section 2.4 discusses why the critical domain size exists based on the effects of varying the domain size. We discuss the mechanism underlying the dependence of critical domain size on SST using the relationship between circulation and energy budget in section 2.5. Section 2.6 provides a summary and conclusions.

2.2. Model and Experimental Design

We used NICAM (Satoh et al., 2008, 2014; Tomita & Satoh, 2004) for the RCE experiments over a sphere. We examined the dependence on spherical domain size using domains of radii $1/16$, $1/8$, $1/4$, $1/2$, and 1 of Earth; these are referred to as the $R/16$, $R/8$,

R/4, R/2, and R/1 domains (equivalent to square domains with sides of length 1411 km, 2822 km, 5645 km, 11290 km, and 22581 km), respectively. Reed and Medeiros (2016) studied RCE using various radii with fixed grid points to investigate the resolution dependency. Here, we fixed a quasi-uniform 14-km horizontal resolution by changing grid points for each radius. The number of grid points is 10×4^5 , 10×4^6 , 10×4^7 , 10×4^8 and 10×4^9 , from the smallest to the largest domain, respectively. This mesh size is coarser than that typically used for cloud-resolving models covering smaller domains but is widely used for NICAM global simulations (Satoh et al., 2014). The coarser simulation reproduces stronger updrafts that mix less with the environment than those in O(km) simulations. That may encourage aggregation, but large-scale organized convective structures such as Madden-Julian oscillations are generally well-reproduced without using cumulus parameterization, even at coarser horizontal resolutions, as shown by Holloway et al. (2013). We used a vertical grid with 38 levels extending to 40 km above sea level; the layer thickness gradually increased with altitude. Cloud microphysics was computed using the single-moment bulk microphysics scheme (Tomita, 2008; Roh & Satoh, 2014). No convective parameterization was used. The turbulent closure was calculated using level 2 of the Mellor-Yamada-Nakanishi-Niino model (Nakanishi & Niino, 2004). The MstrnX scheme was used for the radiative transfer (Sekiguchi & Nakajima, 2008).

Numerical simulations were conducted in the RCE configuration with uniform SST over the spherical domain without rotation. Globally constant SSTs of 290, 295, 300, 305, and 310 K were used as the surface boundary conditions. We refer to these SST experiments as SST290, SST295, SST300, SST305, and SST310, respectively. The solar

insolation was fixed at 551.58 W m^{-2} with a fixed zenith angle of 42.05° , which is the same as those used in RCEMIP. Initial temperature and water vapor profiles were obtained after a spin-up with a single-column version of NICAM using the same SST setting. A random noise perturbation was added to the initial temperature field at the lowest five layers to break the symmetry. Each simulation was run for 150 days. We assumed that all experiments reached an equilibrium state after 100 days. We used the final 50 days for RCE analysis.

2.3. Results

2.3.1. Overview of the Equilibrium Solutions of the Simulations

Figure 2.1 shows the column water vapor (CWV) and precipitation distributions on the last day of the SST300 experiment. CSA was realized from $R/16$ to $R/4$ as a convective cell covering connected areas of high CWV that formed almost a single region. For domain sizes larger than $R/4$, multiple convective regions appear. In all cases, precipitation cells have a finer structure than CWV regions, and multiple regions of intense precipitation exist in a convective region defined by CWV. We focus on the structure based on CWV, which has the largest horizontal scale. The critical domain size is defined as the largest domain size that allows only a single convective region. The detailed estimation is provided in section 2.3.2; we can see that the critical domain size is between $R/4$ and $R/2$ in SST300 (Fig. 2.1). The area of the $R/4$ experiments corresponds almost to that of a square domain with sides of 5000 km; thus, the critical domain size captured by the present experiment is close to that of previous studies using a square domain (Arnold & Putman, 2018; Patrizio & Randall, 2019).

The results for the other SSTs are shown in Supplementary Figure A2.1-A2.4. The critical domain size is between $R/4$ and $R/2$ except SST290. In SST290, there are multiple convective regions at $R/4$ clearly and a single convective region at $R/8$. Except for SST290, multiple convective regions appear for domain sizes larger than $R/4$. Note that multiple convective regions at $R/4$ in SST295 are temporary and will become one cluster after some days. The convective region was circular for $R/16$ and $R/8$, relatively band-shaped for $R/4$, and a mix of circular and band-shaped for $R/2$ and $R/1$. This difference in the shape of convective clusters between domain sizes suggests that convective regions tend to be more band-shaped as domain size increases. Convective regions are not stationary but instead, change their shape, and internal precipitation systems also evolve over time. The dependence of CSA on cluster shape has been discussed in previous studies, which showed the complexity of the dependency of shapes (e.g., Holloway & Woolnough, 2016). We will not examine the shape of convective regions and their dependence on domain size in this thesis. Although it may be better to consider the shape of the convective region when referring to the horizontal scale, in this study, we simply define the horizontal scale of the convective region as the square root of the region's area. We have defined the convective region using the CWV threshold. We will explain the threshold later.

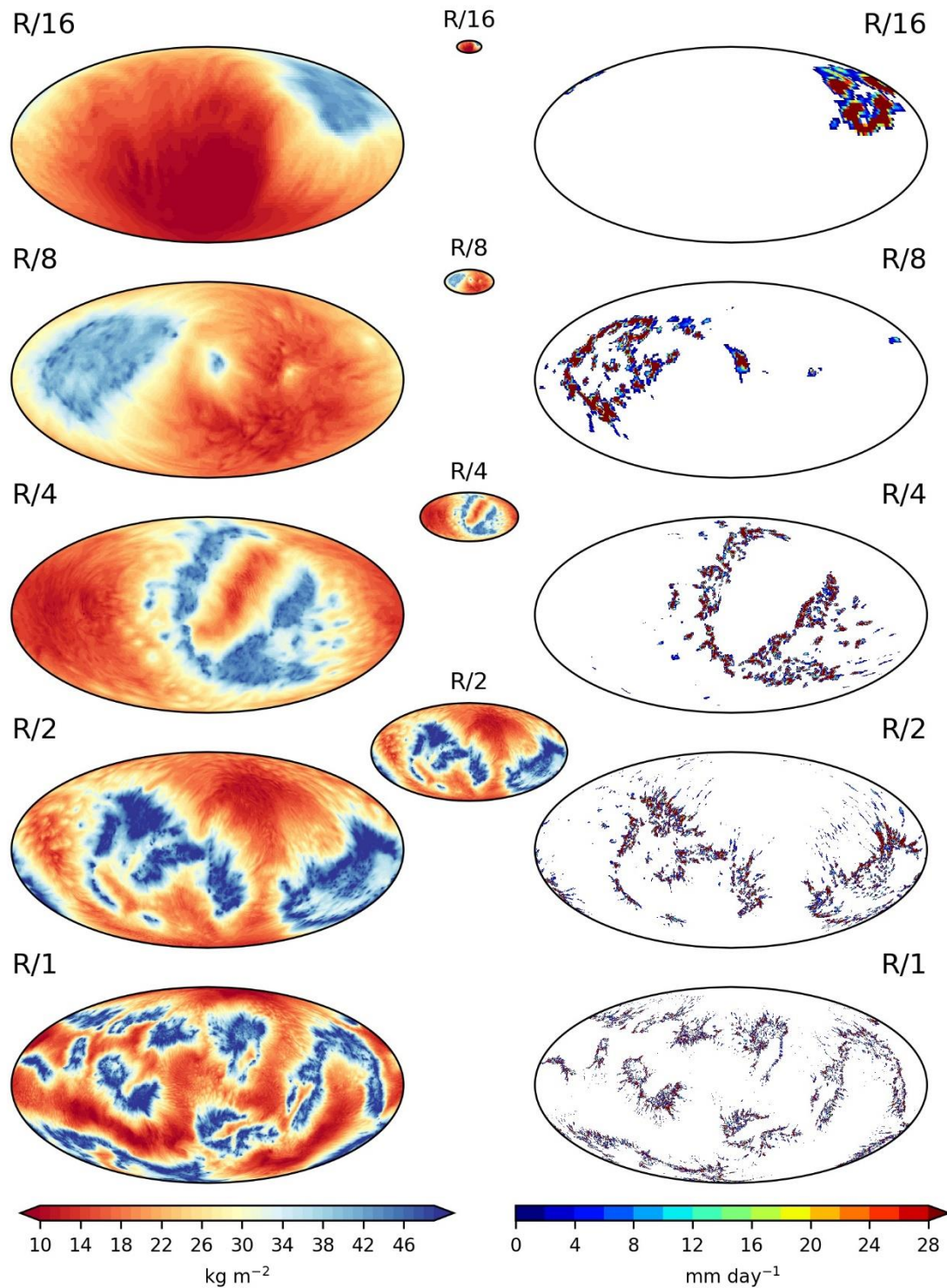


Figure 2.1. Snapshots of daily average (left) column water vapor (CWV) and (right) precipitation at day 150 for domain sizes (from top to bottom) $R/16$, $R/8$, $R/4$, $R/2$, and $R/1$, where R is the radius of Earth in SST300. The left and right panels are zoomed in. The center panel shows the scale of each simulation with respect to $R/1$.

Figure 2.2 shows the time evolution of the global average CWV in SST300. Since the initial profile is relatively moist, the domain-averaged CWV decreases at the onset of CSA (day 20) when the contrast between moist convective regions and dry subsidence regions becomes distinct. CWV then gradually increases for domain sizes of $R/4$ and larger. After day 100, CWV becomes almost quasi-equilibrated and increases with domain size. For $R/16$, CWV oscillates after day 40 for about 20 days; such oscillations exist in RCE results with other models (e.g., Patrizio & Randall, 2019) and may be an interesting aspect of RCE. However, we do not examine the mechanism of these oscillations in this study; we focus only on the quasi-stationary fields. We analyzed days 100 to 150 and confirmed that the quasi-steady state is reached after day 100 at other SSTs (not shown).

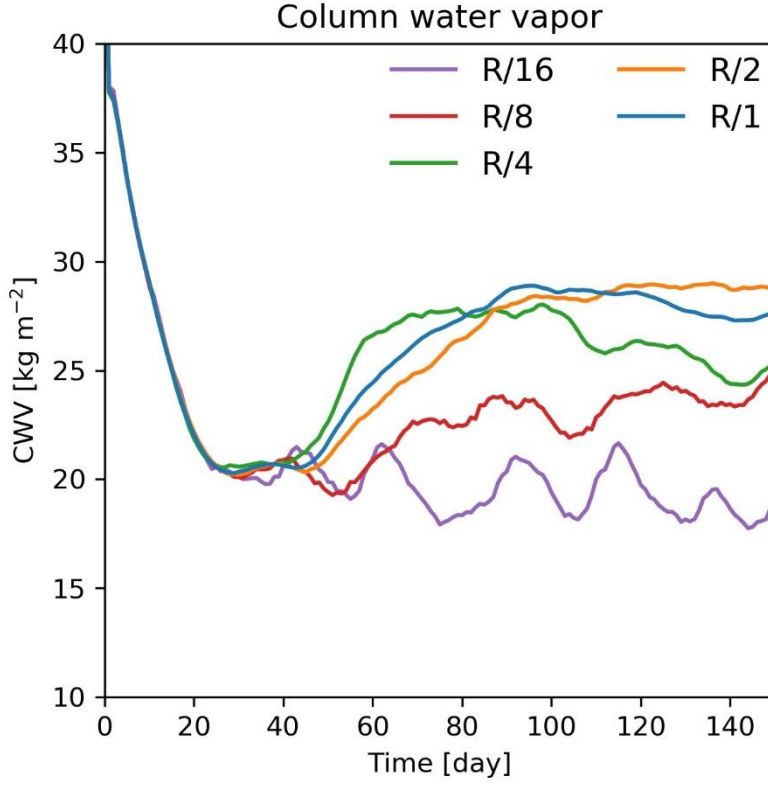


Figure 2.2. Time evolution of global average CWV in SST300 for domain sizes $R/16$ (purple), $R/8$ (red), $R/4$ (green), $R/2$ (orange), and $R/1$ (blue).

Next, we investigate the dependence of the vertical structure of global average fields on domain size (Fig. 2.3). The global average temperature gradually increases in the free troposphere as domain size increases (Fig. 2.3a). However, this increase stops almost completely at $R/2$ and $R/1$, indicating convergence of the global average physical quantities. As the temperature increases, the tropopause rises. These temperature responses indicate that the temperature profile becomes closer to a warmer, moist adiabat at a sufficiently large domain size. The relative humidity increases in the low and middle troposphere. As the tropopause rises, it becomes drier around 10–13 km (Fig. 2.3b). Figure 2.3c shows that the melting level at around 4–5 km increases with increasing domain size. The amount of condensate in both the liquid and solid hydrometeors

increases with domain size. The altitude of the cloud top increases with the rising tropopause, and the anvil cloud fraction at around 12–13 km is not significantly sensitive to domain size (Fig. 2.3d). The sensitivity to domain size of features such as moistening and warming is the same as in previous studies (Arnold & Putman, 2018; Patrizio & Randall, 2019). The convergence of the equilibrium state is achieved larger than a critical domain size.

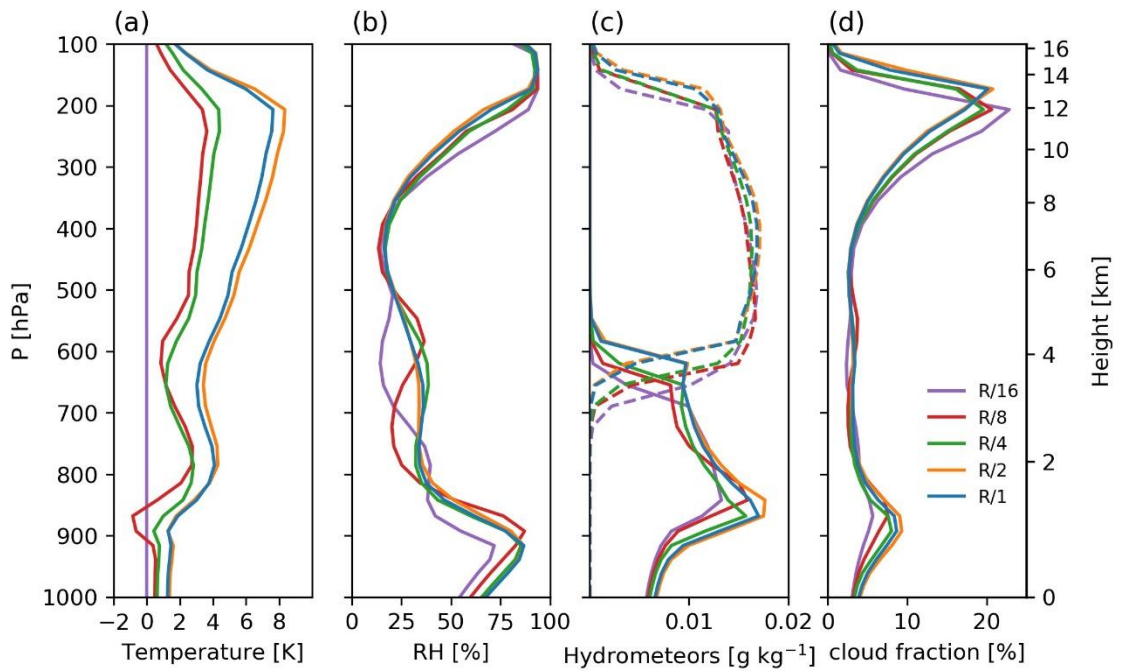


Figure 2.3. Dependence of global average fields on domain size as a function of pressure in SST300 for a) the difference in temperature from R/16, b) relative humidity, c) mass concentrations of liquid hydrometeors (solid) and ice hydrometeors (dotted), and d) cloud fraction. These values are averaged over the analysis period (100–150 days).

2.3.2. Critical Domain Size and Natural Horizontal Scale of Convective Region

The results shown in Figure 2.3 indicate a critical domain size above which physical quantities converge. A comparison of Figures 2.1 and 2.3 suggests that multiple convective regions exist in the convergent regime, in which the domain size is larger than $R/4$. Thus, we can estimate the critical domain size from the convergence of the global

average quantities. From the snapshots (Fig. 2.1), we can infer that the critical domain size is between $R/4$ and $R/2$, but the precise value may depend particularly on SST. We estimate the critical domain size using the global average CWV and the mass-weighted column-averaged temperature (CAT) to represent the temperature and water vapor fields. We have chosen these variables to represent the atmospheric field in an RCE system. In addition, the convergence of CWV standard deviation (CWVstd) and precipitation was also examined. Figure 2.4 shows the relationship between the global average of CWV, CAT, CWVstd, and precipitation and the domain size for SSTs tested in this study. In all cases, their values almost converge for $R/1$ and $R/2$. We can define the critical domain size using them as the intersection of the converged value and the logarithmically fitted $R/16$, $R/8$, and $R/4$. The fitting was done for each of them. This definition of critical domain size is sufficient for the present discussion but should only be considered a first approximation. Ideally, one would search for a more accurate value by varying the domain size with finer increments. Note that we use the same horizontal grid spacing for all cases. The combination of grid spacing and domain size is limited for the NICAM simulations over a spherical geometry.

The estimated critical domain sizes are summarized in Table 2.1. The critical domain size is largest in SST295 and 300 and smallest in SST290. However, it is unnaturally large for SST 300 using CWVstd and precipitation. The snapshots (Fig. A2.1) suggest the existence of multiple convective regions for $R/4$ in SST290, as can be inferred from Figures 2.4b, 2.4d, 2.4f, and 2.4h (cyan dots). For cases of warmer SST (SST305 and 310), the critical domain size becomes smaller than that in SST295 and 300. Although there is uncertainty in the estimated critical domain size for using variables, the dependence of critical domain size on SST is the same. The existence of the critical

domain size and the non-monotonic dependence of the critical domain size on SST are discussed further in sections 2.4.1 and 2.4.2, respectively.

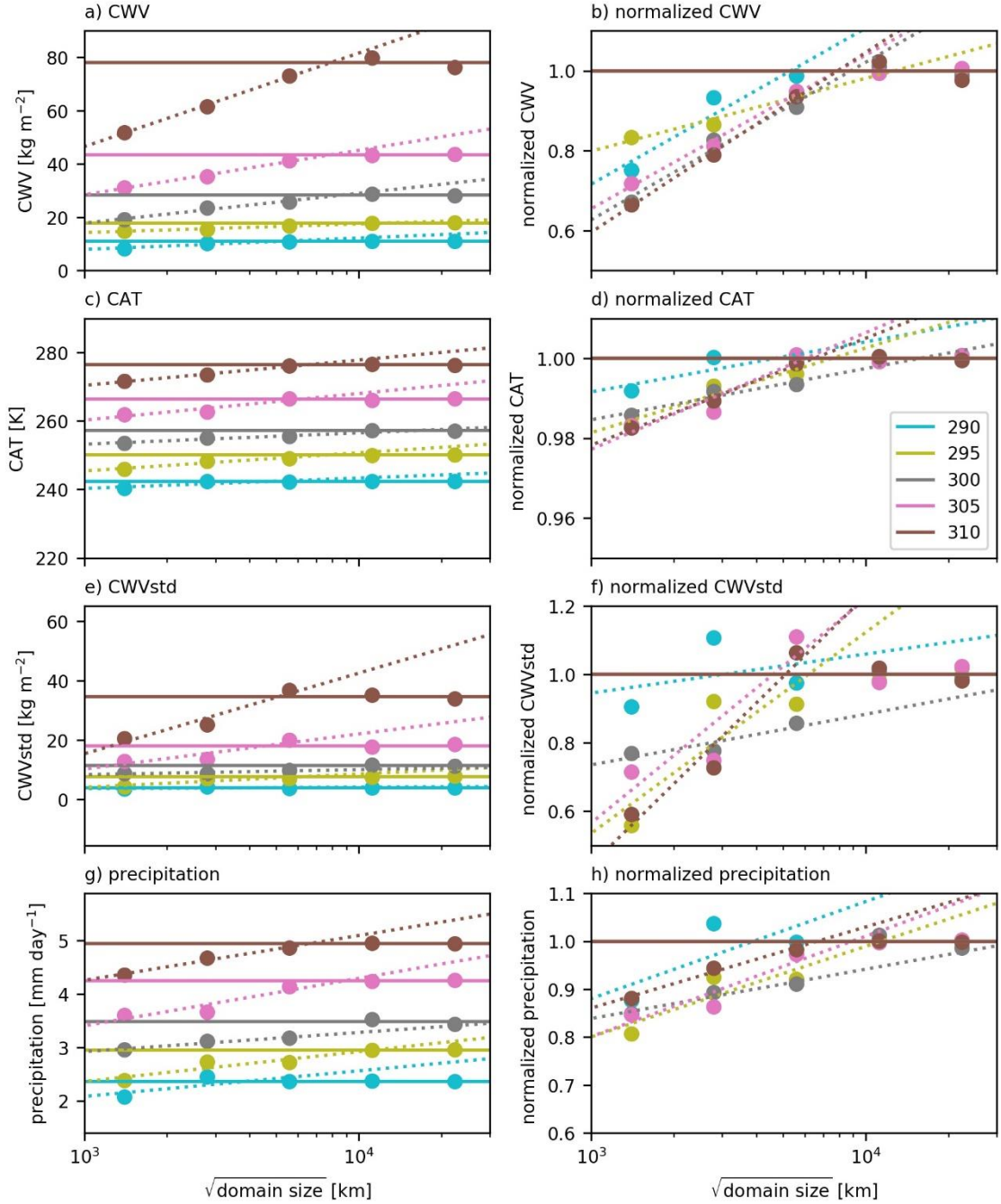


Figure 2.4 Global average (a, b) column water vapor (CWV), (c, d) mass-weighted average column-averaged temperature (CAT), (e, f) standard deviation of CWV (CWVstd), and (g, h) precipitation. (b), (d), (f), and (h) are the same as (a), (c), (e), and (g), respectively, but normalized to the mean of $R/1$ and $R/2$. The dotted lines show the

logarithmic fitting line for $R/16$, $R/8$, and $R/4$. Solid lines show the mean of $R/1$ and $R/2$. The colors indicate SST290, 295, 300, 305, 310; cyan, olive, gray, pink, and brown, respectively.

Table 2.1. Critical Domain Size and Natural Scale of Convective Region. CWV is column water vapor. CAT is mass-weighted average column-averaged temperature. CWVstd is the standard deviation of column water vapor.

SST [K]	Critical Domain Size [km]				Natural Scale of Convective Region [km]			
	CWV	CAT	CWVstd	Precipitation	CWV	CAT	CWVstd	Precipitation
290	5348	4713	3032	3905	2135	1882	1211	1559
295	12715	7567	6192	11373	4983	2965	2426	4457
300	8833	15795	60982	36872	3596	6431	24829	15013
305	7905	6029	4630	8903	2616	1995	1532	2946
310	7910	6503	5112	6666	2946	2421	1904	2482

Multiple convective regions co-exist at a sufficiently large domain size, such as $R/1$ or $R/2$. In such situations, we can define the natural scale of the convective region as a representative scale of the convective region. We believe that the natural scale of the convective region is achieved in a simulation above the critical domain size. However, when there are multiple convective regions, they do not necessarily represent the natural scale of the convective region. In cases where we know what fraction of the region is convective, we can consider the natural scale of the convective region to be the size of the convective region at the critical domain size.

The threshold of CWV is defined for each experiment based on the relationship between CWV and vertical velocity. Figure 2.5a shows the mass-weighted average vertical velocities sorted by CWV in SST300. Moist categories of CWV correspond to

regions of upward motion, while drier categories correspond to regions of downward motion. The boundary of the convective region is defined at the CWV point at which the mass-weighted average vertical velocity is zero. Figure 2.5b shows the relationship between the estimated CWV boundary value (circle) and the frequency distribution of CWV. The estimated CWV threshold corresponds to the saddle of the frequency distribution. This shape of the probability function of CWV is similar to that found in observational studies (Mapes et al., 2018; Masunaga & Mapes, 2020). As for the histogram itself, as domain size increases, the frequency of higher CWV values increases, and lower CWV values decrease. This dependence of CWV on domain size is consistent with the results shown in Figure 2.2, in which the global mean CWV increases as domain size increases.

Figure 2.5c shows the fraction of the whole domain that comprises the convective region, calculated by the CWV threshold for each SST and the domain size. This fraction is represented as a single convective region up to and including $R/4$ and as multiple convective regions for more than $R/4$. As domain size increases, the fraction of the convective region tends to increase, except in SST295; it is almost constant at $R/1$ and $R/2$, indicating convergence. However, it should be noted that this is the fraction of the total area of the convective regions, not the scale of individual convective regions.

The natural scale of the convective region could be estimated by multiplying the critical domain size with the fraction of the convective region (the average of $R/1$ and $R/2$; Table 2.1). This fraction is 11–17 % at $R/2$ and $R/1$ (Fig. 2.5c). Therefore, the dependence of the natural horizontal scale of convection on SST is similar to that of the critical domain size. This dependence does not change for other convective region indicators, such as meso-convective fraction (Muller & Held, 2012; Patrizio & Randall, 2019). The natural

scale tends to be maximum in SST300 and SST295 and is smaller in SST290, SST305, and SST310.

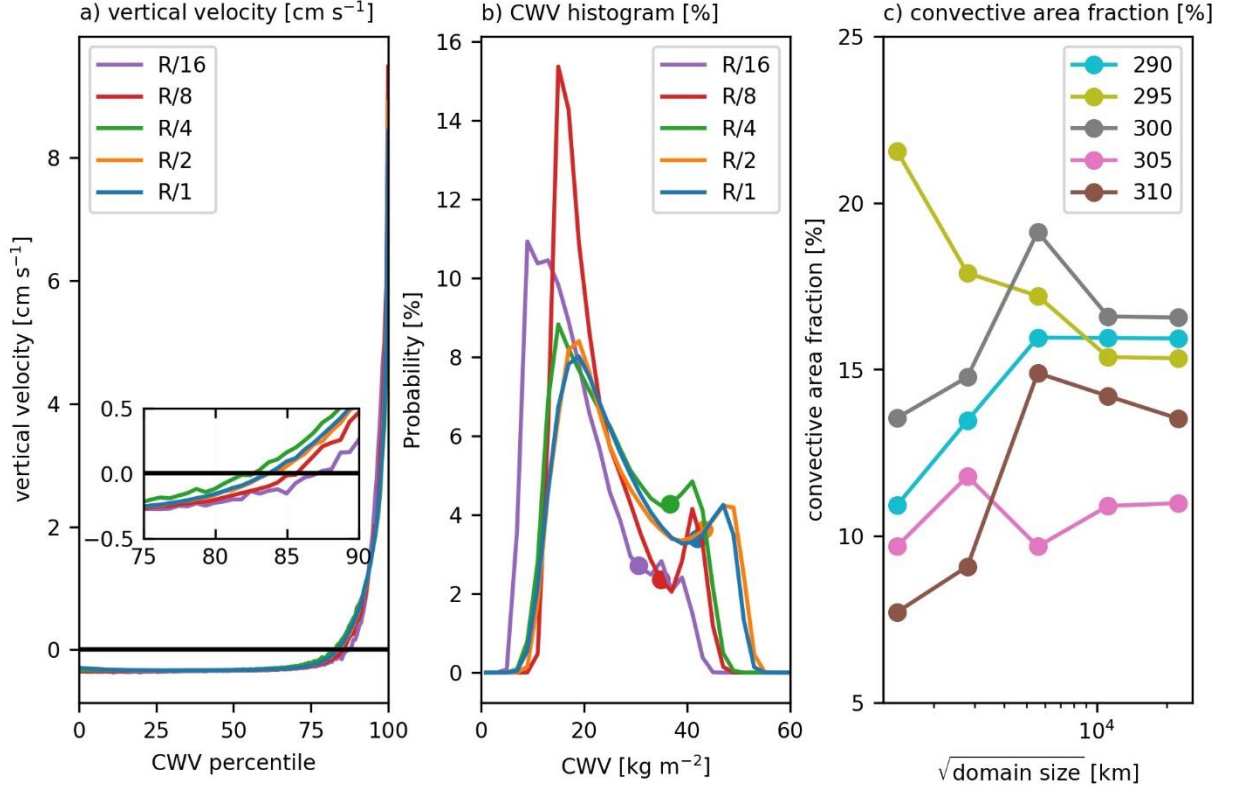


Figure 2.5. (a) Mass-weighted average vertical wind velocity sorted by the CWV. (b) Histogram of CWV with a bin size of 1 kg m^{-2} . Circles indicate threshold values. (a) and (b) are shown for different values of domain size in SST300. (c) Convective area fraction as a function of the square root of domain size [km] for different values of SST.

We introduce another measure of the natural scale of the convective region to support our finding that the dependence of the scale of the convective region on SST is non-monotonic and reaches a maximum at an SST of around 300. We define single connected regions of CWV using a connected-component labeling algorithm to label grids in which CWV is above the threshold with four connectivity (i.e., two grids belong to the same label only if they share a common side). Then, we measure the horizontal scale of the convective region for $R/2$ and $R/1$ by labeling and measuring the size of single

connected regions of CWV over the threshold. Figure 2.6a shows an example of the result of the connectivity of CWV (same time step as in Fig. 2.1). Although the labeling separates large convective regions, convective regions that have not yet grown to the natural scale are temporarily separated from other convective regions or merged with larger ones. Large convective regions form a banded structure, while small regions are relatively circular. We defined the convective region of the 800 largest areas for $R/1$ by removing the effects of smaller areas that do not reach the natural scale of convection; this corresponds to 16 convective regions per time step, as we take measurements at 50-time steps. We implicitly assume that there are at least 16 natural convective regions for $R/1$ at one time step since the surface of $R/1$ is 16 times larger than that of $R/4$, which has a single region. We chose the top 200 areas for $R/2$ because the surface of $R/1$ is four times larger than that of $R/2$. Figure 2.6b shows the frequency distributions of the number of convective regions as a function of their scale, defined by the square root of the area of convective regions for $R/1$. There are many clusters below the scale of 500 km, as indicated by dotted lines. Solid lines in Figure 2.6b show the histograms of the 800 largest areas.

The maximum scale of the convective region is about 6000 km in SST305; this may be an exceptional case due to the temporary merging of convective clusters. Figure 2.6c shows the dependence of the mean and the median scales of the 800 (200) largest convective regions for $R/1$ ($R/2$) on SST. The scale increases from an SST of 290 K to an SST of 300 K, at which it reaches a maximum, and decreases toward an SST of 305 K. The largest mean and median scales are in SST310 in $R/2$; this is different from the results shown in Table 2.1, indicating that ambiguity remains for definitions of the scale of convective regions. Both the mean and the median scales differ between $R/1$ and $R/2$ by

about 500 km, although there is a convergence of a physical quantity for domain sizes larger than the critical domain size (Fig. 2.4). When the domain size is larger than the critical domain size, the convective region's horizontal scale is within a range that is smaller than the maximum possible scale. In addition, it is possible to increase the number of convective regions. As a result, the size of each convective region at $R/1$ is smaller than at $R/2$. However, the dependence on SST is the same except for SST310 at $R/2$.

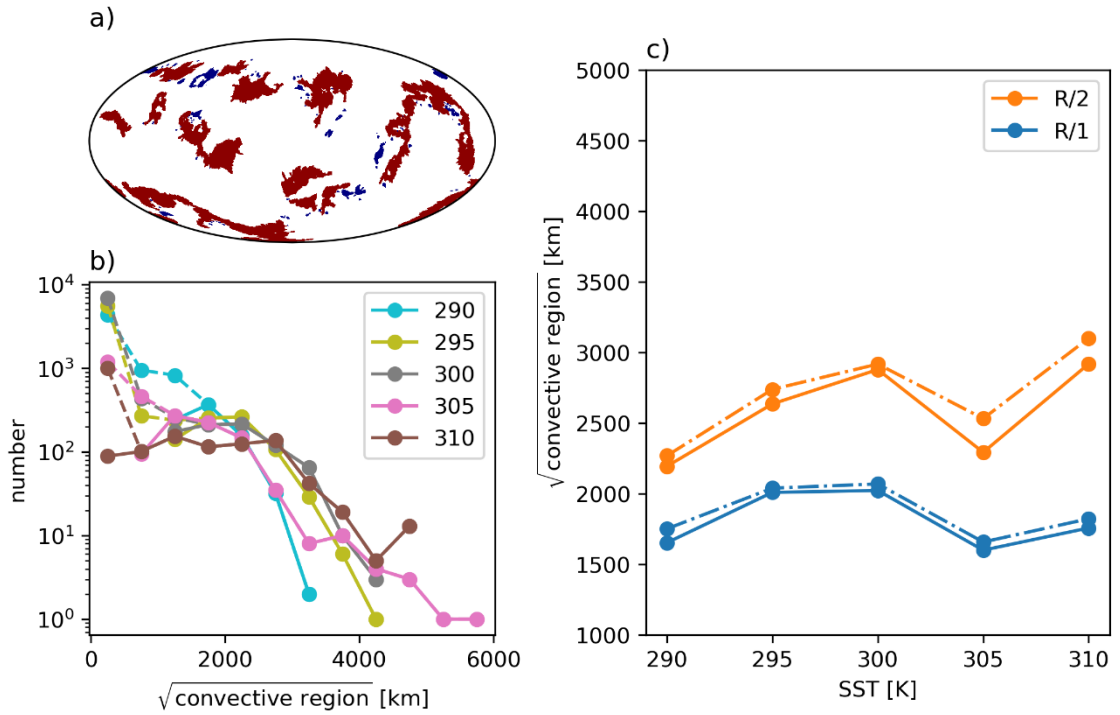


Figure 2.6. (a) Snapshot of the labeled convective region in SST300 for $R/1$ on day 150. Dark red shows large convective regions (defined as the 800 largest convective regions), and navy shows the remaining small convective regions. (b) Histogram of labeled convective regions for $R/1$ as a function of the square root of the area of convective regions. Dashed lines show histograms for all the labeled convective regions. Solid lines show histograms for the 800 largest areas. (c) Dependency of the mean (solid) and median (dashed) scales of the 800 ($R/1$) or 200 ($R/2$) largest areas of labeled convective regions on SST.

We examined the dependence of the critical domain size on SST using multiple methods by estimating from the convergence of physical quantities or connected convective regions. This dependence on SST is the same as that of the natural scale of the convective region. The natural scale of the convective region is between 2000 km and 6000 km for all indices. This result suggests a limit to the extent to which the convective region can expand spontaneously. The natural scale of the convective region is relatively large in SST295 and SST300 and small in SST290, SST305, and SST310, indicating that it may not increase or decrease monotonically with SST.

2.4. Why Does Critical Domain Size Exist?

We have seen that multiple convective regions co-exist under a sufficiently large domain size, such as $R/1$ or $R/2$, for any SST experiment. In this section, we investigate why the critical domain size exists. In other words, we examine why a single convective region has an upper size limit and cannot expand to a large single convective region at domain size $R/1$ or $R/2$.

2.4.1. Spatial Variance of FMSE Budget

Following Patrizio and Randall (2019) regarding the relationship between CSA and domain size, we use the budget equation for the spatial variance of the frozen moist static energy (FMSE). The FMSE is defined by

$$h = c_p T + gz + L_v q_v - L_f q_i \quad (2 - 1)$$

where c_p is the isobaric specific heat, T is the temperature, g is the acceleration due to gravity, z is the height, q_v is the water vapor mixing ratio, q_i is the ice condensate mixing ratio, L_v is latent heat of vaporization, and L_f is the latent heat of fusion. The column net

radiative flux (RAD), the sum of latent and sensible heat release from the surface (SEF), and horizontal convergence of the flux of h are the only terms that can alter the column integral of h :

$$\frac{\partial \langle h \rangle}{\partial t} = RAD + SEF - \nabla_h \cdot \langle hu \rangle \quad (2-2)$$

The angular brackets denote a density-weighted vertical integral from the surface to the top of the model. Following Wing and Emanuel (2014), we can derive

$$\frac{1}{2} \frac{\partial \langle h \rangle'^2}{\partial t} = \langle h \rangle' RAD' + \langle h \rangle' SEF' - \langle h \rangle' \nabla_h \cdot \langle hu \rangle \quad (2-3)$$

Here, a prime denotes a departure from a global average value. Globally averaging and normalizing each term by $\overline{\langle h \rangle'}$ yields the growth rate of $\langle h \rangle$ variance.

We focus on the quasi-equilibrium state in this study and compare the global average quantities from day 100 to day 150. Figure 2.7 shows the global average FMSE budget terms. Our study is not much different from previous RCE studies in the FMSE budget view. The term RAD is always positive, indicating that it contributes to the maintenance of CSA, while the convergence term is negative, i.e., contributing to damping; SEF is primarily positive but decreases as domain size increases and is negative at some SSTs or domain sizes. The difference in RAD between simulations for the same SST is slight. The atmospheric longwave cooling in the convective region decreases due to clouds, and enhanced moisture relative to the dry region by increasing shortwave heating tends to maintain CSA. The relative contribution of the surface flux term in the total diabatic process becomes weaker than that of the radiation term as domain size increases.

The convergence term is negative, and its magnitude approaches zero as domain size increases. The convergence term indicates that the FMSE is exported from the

convective region but decreases as domain size increases. Patrizio and Randall (2019) hypothesized that the critical domain size might occur where the convective region switches from exporting FMSE to importing FMSE. This study shows a similar decrease in FMSE export as domain size increases. However, it does not change sign, i.e., we do not have a case of FMSE being imported to the convective region above the critical domain size. The decrease in FMSE export from the convective region occurs regardless of SST. The decrease in FMSE export is related to an increase in detrainment in the middle layer, as shown below. The decrease in FMSE export makes the convective region wetter when domain size increases.

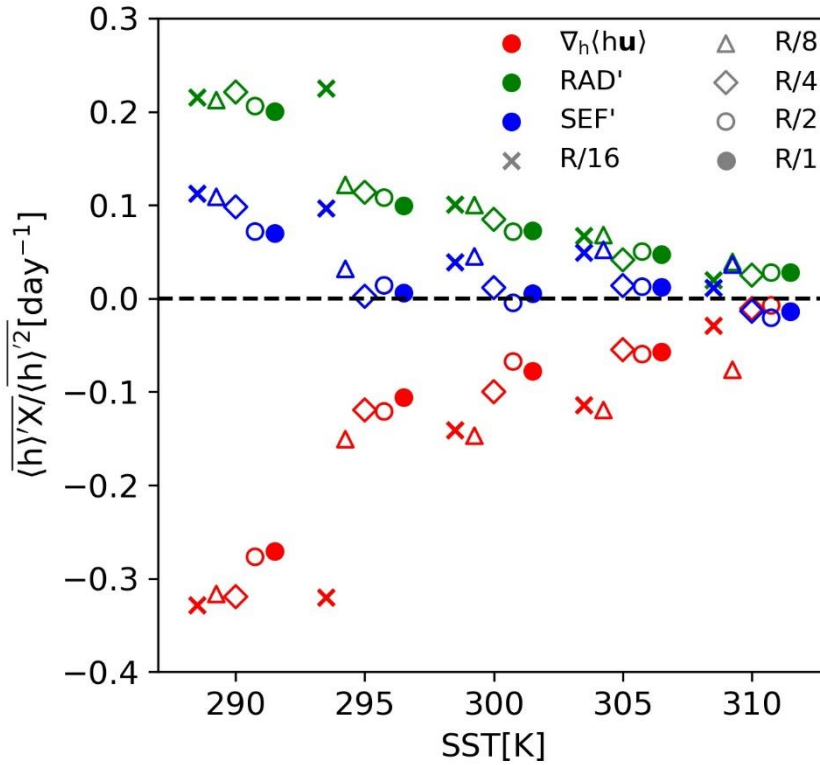


Figure 2.7. Domain averages of three terms on the right side of equation (2-3) normalized by the domain average of the covariance of $\langle h \rangle$ expressed in units per day. The horizontal convergence of the flux of $\langle h \rangle' \nabla_h \cdot \langle h \mathbf{u} \rangle$ is the residual calculated at each time step. Markers show the domain size of each simulation for days 100-150.

2.4.2. The Domain Size Dependence of Boundary Layer and Energy Balance

We analyzed the lateral structure of the boundary layer sorted by CWV, following the analysis method used in previous studies (e.g., Bretherton et al., 2005). This analysis averaged physical quantities over a 4×4 grid (approximately $56 \text{ km} \times 56 \text{ km}$). Here, we show only the results of SST300; the dependence of the equilibrium states on domain size is similar for the other SSTs tested (not shown).

Figure 2.8 shows the lateral distributions of the quantities near the surface as a function of CWV. As domain size increases until $R/2$, the 10 m wind speeds (Figure 2.8a), the temperature and the specific humidity at the lowest model level (Fig. 2.8b and 2.8c), and the latent heat flux (LHF; Fig. 2.8d) increase, but they are almost unchanged at $R/2$ and $R/1$. These findings are consistent with those shown in Figure 2.3. The increase in 10 m wind speed until domain size reaches $R/2$ is due to the increase in the subsidence region when domain size increases. The warmer temperature in the convective region than in the drier region increases the horizontal pressure gradient, which needs to sustain enhanced wind speed. These tendencies are consistent with previous studies conducted on square domains (Arnold & Putman, 2018; Patrizio & Randall, 2019; Yang, 2019). Despite the moistening in the boundary layer, the LHF increases due to increased wind speed. The upper limit of LHF is proportional to the domain-averaged precipitation, which is constrained by the net radiative cooling. We conclude that such a tropospheric energy balance constrains the surface wind speed and determines the critical domain size.

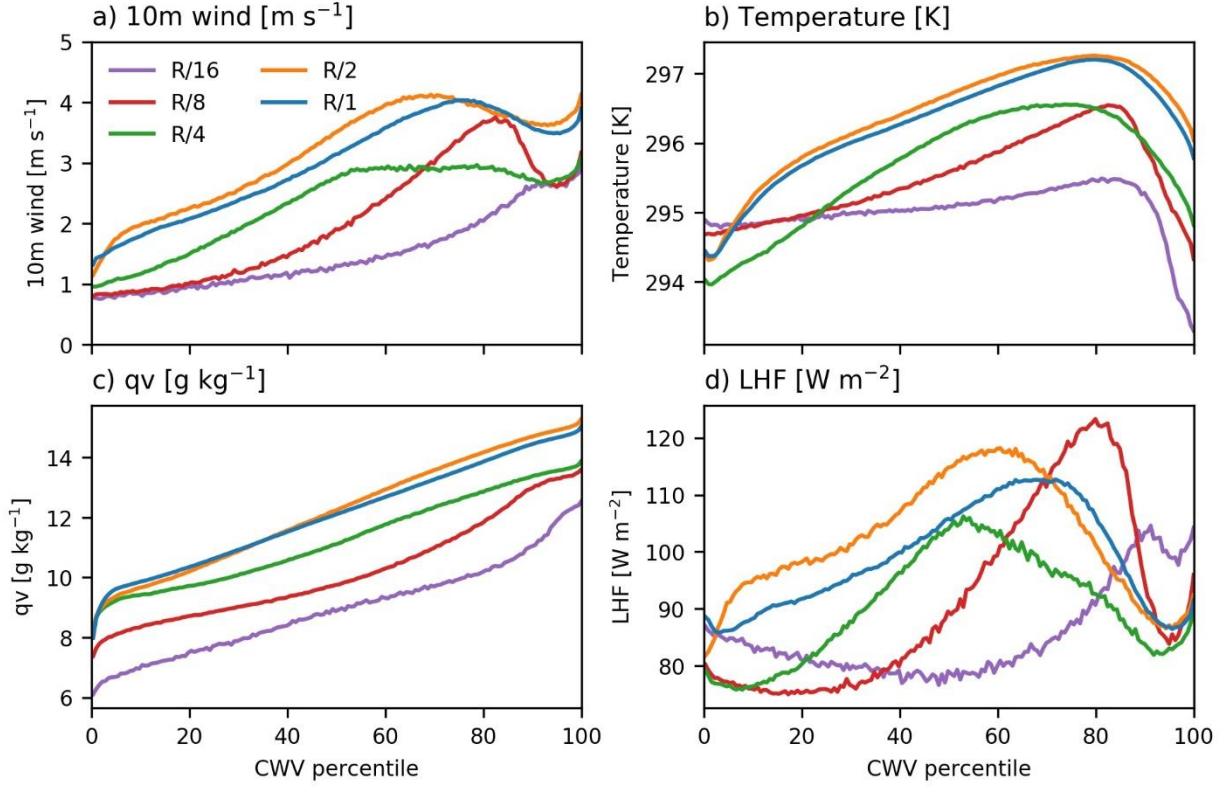


Figure 2.8. (a) 10 m wind speed, (b) temperature of the lowest model level, (c) specific humidity of the lowest model level, and (d) latent heat flux sorted by CWV for five different domain sizes in SST300, using daily mean values averaged over the analysis period.

We show here how the critical domain size is determined under the constraint of the energy budget. Assuming that domain-averaged column-integrated radiative cooling is Q and surface evaporation is E , we can approximate the following balance in the RCE by neglecting the surface sensible heat flux:

$$Q(A) = L_v E \quad (2 - 4)$$

where A is the domain size. Sensible heat flux accounts for a relatively large fraction of the surface energy flux when SST is low (Fig 2.9e and 2.9f; e.g., SST290) but still less than latent heat flux. In addition, the change in sensible heat flux with domain size is

smaller than the latent heat flux. Therefore, the sensible heat flux can be neglected. The evaporation is calculated using the bulk wind speed U ,

$$E = C\Delta q(A)U(A) \quad (2-5)$$

where C is the bulk coefficient, and Δq is the difference in water vapor between the surface and lowest model level. We have seen that U increases with domain size (Figure 2.9a). Let us assume that this dependency is approximated as a linear relationship:

$$U(A) = B A \quad (2-6)$$

where B is the proportionality coefficient. This relationship is also used by Arnold and Putman (2018). At the critical domain size A_c , we denote $Q(A_c) = Q_c$ and $\Delta q(A_c) = \Delta q_c$. Then, the critical domain size is given by:

$$A_c = \frac{Q_c}{\Delta q_c} \frac{1}{L_v C} \frac{1}{B} \quad (2-7)$$

Figure 2.9a shows the dependency of the bulk wind speed defined by Eqs. (2-4) and (2-5) with $C = 1.0 \times 10^{-3} [\text{m s}^{-1}]$. The bulk wind speed U increases similarly to the 10 m wind speed (Fig. 2.8a) for domain sizes smaller than the critical domain size, which stays almost constant above the critical domain size. Figures 2.9b and c show the dependence of Q and Δq on domain size, respectively; Q increases and Δq decreases with increasing domain size for all SSTs. Precipitation and latent heat fluxes also increase to balance this change (Fig. 2.9c and 2.9d). Both Q and Δq increase with SST at any domain size.

The reason why the critical domain size exists can be summarized as follows. In a single convective region for domain sizes less than $R/2$, surface wind speed increases as domain size increases because the distance between the convective and dry regions becomes large. The change in surface wind speed matches the increases in temperature

and humidity. The vertical temperature profile (Fig. 2.3a) and the height of the tropopause increase, but the moist adiabat constrains them. Thus, moist adiabat and surface temperature constrain the warmest temperature profile. That places an upper limit on net radiative cooling if relative humidity does not change significantly. The change in radiative cooling concerning the domain size is dominated by the clear sky radiation, and the effect of cloud radiation interactions is insignificant (Fig 2.9g and 2.9h). Warming associated with domain size expansion increases longwave radiative cooling and shortwave radiative heating (Fig. 2.9i and 2.9j). The increase in longwave cooling is greater than shortwave heating, resulting in a net increase in radiative cooling. The latent heat flux will also have an upper limit because of the balance with the radiative cooling (Fig. 2.9b and 2.9f). The latent heat flux increases with domain size despite the decrease in Δq (Fig. 2.9c). Therefore, latent heat flux is controlled mainly by wind speed. The upper limit to the latent heat flux and the strong relationship between latent heat flux and surface wind speed indicate that the surface wind speed must have an upper limit. This energy constrain indicates that domain sizes allowing only a single aggregated convective region must also have an upper limit. When the domain size exceeds such critical domain size, another convective cluster must form because the circulation caused by a single cluster cannot cover the whole domain. It could still be possible that a larger cluster exists at a large domain size, organized in a long band (snake-like structure), as then the distance between the convective and dry regions would still be relatively small. However, suppose the individual convection in the convective region (CWV field) behaves randomly. We speculate that the band-shaped convective region may fluctuate and merge with other convective regions at a point of large curvature, then become close to circular. Therefore,

we believe there may be a temporary banded structure, but it is unstable. It may produce the critical horizontal scale of the convective region when time is averaged.

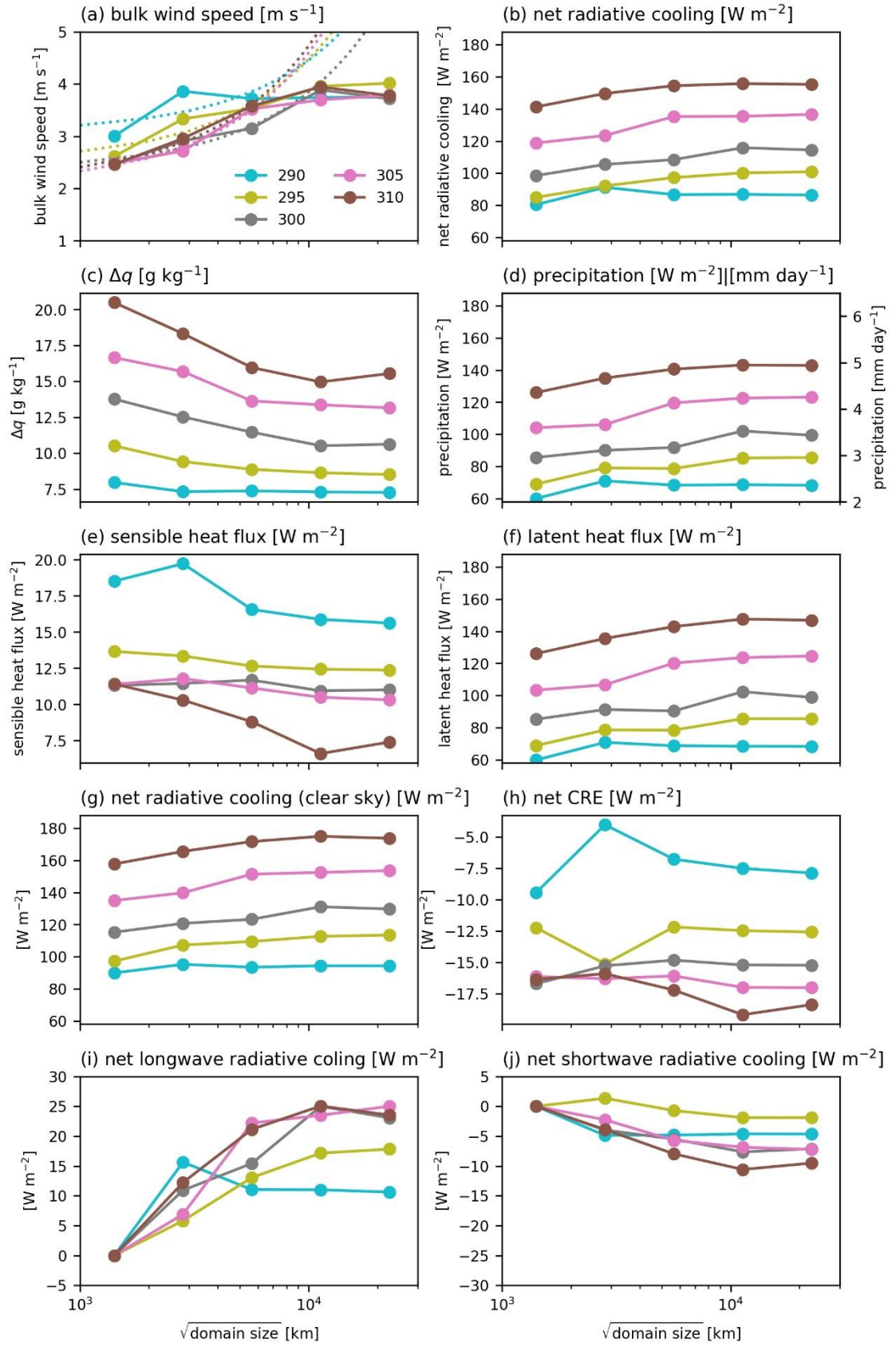


Figure 2.9. Dependence of (a) bulk wind speed, (b) net radiative cooling, (c) Δq , (d) precipitation, (e) sensible heat flux, (f) latent heat flux, (g) net clear-sky radiative cooling, (h) cloud radiative effect, (i) net longwave radiative cooling, and (j) net shortwave radiative cooling on the domain size for various values of SST. Dotted curves in (a) show the linear fitting of $R/16$, $R/8$, and $R/4$.

2.5. The SST Dependency of Critical Domain Size

We found that the critical domain size does not monotonically change with SST. This section discusses how the dependence of critical domain size on SST is determined. As investigated in the previous section, the dependence of surface wind speed on domain size is essential for determining the critical domain size. We show that such a dependency is closely related to the effective structures of overturning circulation and its dependence on convective activity and SST. We constructed the mass stream function following Bretherton et al. (2005) to investigate the circulation structure. The effective mass stream function ψ is calculated as an integral over vertical velocity with respect to the CWV percentile:

$$\psi_i(z) = \psi_{i-1}(z) + [\rho(z)w(z)]_{i-1} \quad (2-8)$$

where ρ , w , and z are density, vertical wind speed, and height, respectively; the subscript i denotes the i th CWV bin. This method enabled us to characterize the convective detrainment associated with convective mass circulation, although we should note that the topology of the circulation was destroyed in this analysis, as mentioned by Bretherton et al. (2005).

The circulation structure can be determined approximately from the distribution of radiative cooling. As SST increases, the height of the melting level increases, as does the height of the detrainment of water vapor from the convective region. Mid-tropospheric detrainment from the convective region is caused by increased mid-level static stability,

which in turn is due to the melting process described in tropical observational studies (e.g., Johnson et al., 1999; Yasunaga et al., 2006) and RCE studies (e.g., Patrizio & Randall, 2019; Posselt et al., 2012). The detrainment enhances the vertical moisture gradient at the melting level. Because radiative cooling is related to a vertical moisture gradient (Fig. A2.5), it peaks around the melting level and the top of the boundary layer. In addition, there is a minimum of radiative cooling below the melting level. There is a strong correlation between the height of the melting level and the height of the peak in the radiative cooling at the middle troposphere. Thus, the midlevel peak of radiative cooling shifts upwards as the melting level increases with increasing SST (Fig. 2.10). In SST290, the melting level is close to the top of the boundary layer (about 2000 m). In SST295 and SST300, the melting level is about 3000–5000 m and is detached from the top of the boundary layer. Even though the boundary layer and the melting level are separated, they have a shallow circulation in the moisture space from the melting level to the boundary layer. The height of maximum cooling at the top of the boundary layer should coincide with the height of the minimum radiative cooling just below the melting level. Hence, the cooling at the top of the boundary layer is weak near the convective region. In SST305 and SST310, the melting levels are about 7000 m and 9000 m, respectively. The change in melting level with SST is not linear but is larger at higher SSTs. This is because the moist adiabatic lapse rate is smaller at a higher temperature, resulting in a smaller overall lapse rate. The interval between the melting levels and the top of the boundary layer increases since the boundary layer height decreases rather than increases. The radiative cooling near the melting level is no longer associated with the low-level circulation due to the rising melting level. The rising melting level leads to stronger radiative cooling at lower levels. We assume that the change in the structure of

the radiative cooling in the CWV height cross-section is related to the change in the wind speed in the boundary layer. This assumption is inspired by a mass balance between the vertical wind speed and the surface flow from the dry to the convective region (Arnold & Putman, 2018; Wing & Cronin, 2016; Yang, 2018a) and radiative-driven circulation (e.g., Bony et al., 2016). The vertical advection of potential temperature is almost balanced with radiative cooling when the temperature is horizontally homogeneous under RCE simulations. The vertical wind speed in the dry region is controlled by radiative cooling and static stability. Thus, there is a relationship between radiative cooling and surface wind speed.

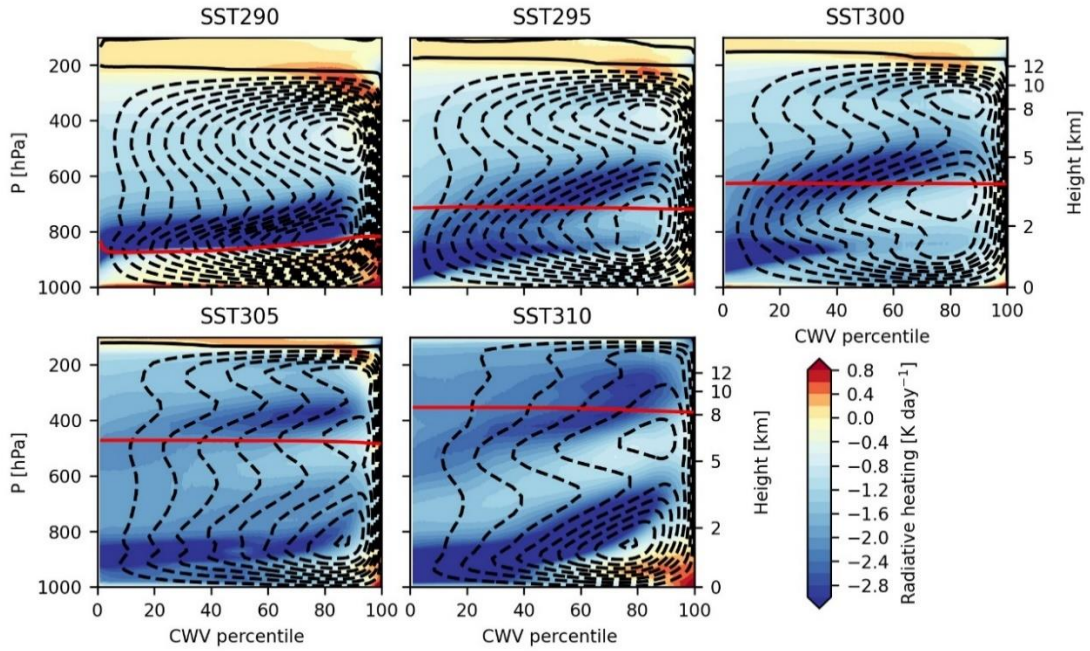


Figure 2.10. Vertical profiles of radiative heating rate, contours of stream function (dashed black lines; anticlockwise every $0.05 \text{ kg m}^{-2} \text{ s}^{-1}$), and contour of freezing level (solid red line) in simulations with different SST at $R/4$.

The radiative cooling can explain the horizontal wind speed at the top of the boundary layer. The radiative-driven vertical wind speed w_r can be estimated as follows (Bony et al., 2016; Ohno & Satoh, 2018):

$$w_r = Q_R \left(\frac{d\theta}{dz} \right)^{-1} \quad (2-9)$$

where Q_R and θ are radiative heating and potential temperature, respectively. Figure 2.11a compares w_r with the actual vertical wind speed at the top of the boundary layer. We choose the 1853 m height because this height is near the top of the boundary layer and without the boundary layer in all SSTs. The vertical gradient of the vertical wind speed is assumed to be small in the dry region. The vertical wind speed almost agrees with w_r in the dry region when the CWV percentile is less than 70.

To estimate horizontal wind speed in moisture space in the boundary layer u_r , we follow Wing and Cronin (2016) and assume that u_r depends on the distance from the central point of the subsidence region. We regard the subsidence region as taking a circular form in which the convective region is located at the edge. From the mass continuity, u_r can be calculated by:

$$u_r = \frac{1}{2\pi r} \int w_r ds \quad (2-10)$$

where r is the radius of the circle, and the integration is done with the moisture space (CWV height cross-section). We assumed $u_r(0) = 0$, where $r = 0$ is the driest region. Figure 2.11b shows that u_r almost agrees with the 10 m wind speed in the dry region with a CWV percentile of less than 60. The 10 m wind speed is enhanced more than u_r near the convective region at CWV percentiles around 80 in SST290, SST305, and SST310. Since the water vapor gradient in the lower layer does not depend significantly on SST (Fig. 2.11c), the increased 10 m wind speed near the convective region mainly enhances

the LHF anomaly (Fig. 2.11d). We speculate that the enhanced surface wind speed near the convective region (SST290, SST305, and SST310) invigorates convective activity. As convection is strong, moisture detrainment from the convective region is enhanced near the melting level. The convective region exports less FMSE when detrainment occurs at a higher level because the middle-level humidity is lower than the boundary layer humidity. This effect increases the horizontal convergence term of Eq. (2-3) with increasing domain size. This effect may be more pronounced in SST290, SST305, and SST310 because the wind speed is enhanced near the convective region as domain size increases in these experiments. That process may lead to a smaller critical domain size by enhancing convective activity, which increases the horizontal convergence of FMSE.

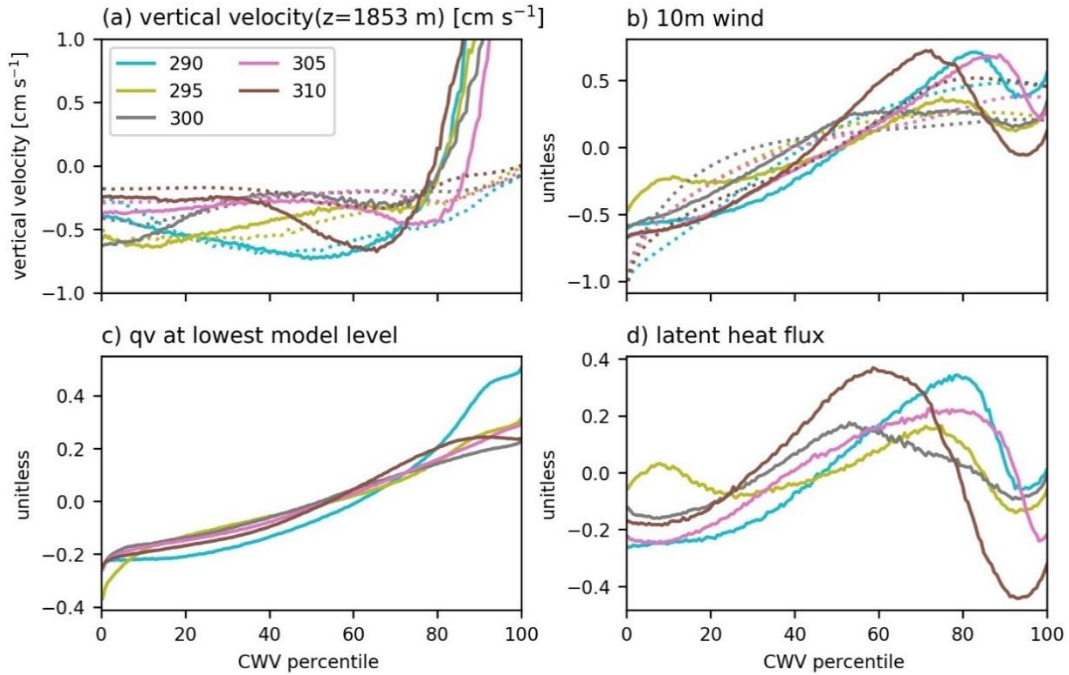


Figure 2.11. (a) Vertical velocity, anomalies of (b) 10 m wind, (c) q_v at the lowest model level, and (d) latent heat flux sorted by CWV in SST290, 295, 300, 305, and 310 at $R/4$ averaged over the analysis period. Anomalies were normalized by the domain average of each value. Dotted lines are the radiatively driven wind speeds (a) w_r and (b) u_r .

The change in the structure of surface winds affects parameter B of Eq. (2-7), which is used for the energy balance in the previous section. The coefficient B is derived from the dependence of bulk wind speed U on area. We use Figure 2.9a to estimate B by fitting the linear relation (Eq. 2-6) for $R/16$, $R/8$, and $R/4$. In SST290, which shows convergence at $R/8$, only the values of $R/16$ and $R/8$ were used. Table 2.2 summarizes the parameters in Eq. (2-7) deduced from the results of the RCE experiments. The critical domain size A_c is not monotonically dependent on SST but is largest for 295 K or 300 K. This result is consistent with the experimental results shown in Table 2.1, indicating the applicability of Eq. (2-7). The dependence of A_c on SST is determined almost by the dependence of parameter B on SST. The precise value of B reflects the structure of the overturning circulation in moisture space. For experiments with warmer SSTs (SST305, SST310) and the coldest SST (SST290), the surface wind speeds were relatively enhanced in the convective region, leading to larger B .

Here, we explain how the surface wind speed pattern in moisture space, which is relatively enhanced in the convective region, is related to larger B . The moisture supply to the convective region becomes greater, and convective activity is enhanced when domain size increases. This process works more efficiently when the wind speed is enhanced near the convective region. Enhancement of convective activity leads to an increase in temperature in the troposphere, contributing to an increase in the radiative cooling Q . This process implies a more significant increase in bulk wind speed to balance the increased radiative cooling. Therefore, B – that is, the rate of increase in bulk wind speed relative to increasing domain size – is larger for the circulation structure with stronger wind speeds in the convective region, such as in SST290, 305, and 310. In

general, $Q/\Delta q$ decreases with increasing SST because Δq increases more, according to Clausius-Clapeyron's law than radiative cooling related to mass flux (Satoh & Hayashi, 1992; Vecchi & Soden, 2007; Satoh, 2013). As $Q/\Delta q$ decreases with an increase in SST, this contributes to the decrease in critical domain size if the change in B is small.

Table 2.2. Parameters in Eq. (2-7). We calculate Q_c and Δq_c as the mean of $R/1$ and $R/2$. B is estimated from the fitting of Figure 2.9a. A_c is calculated by using $C = 1.0 \times 10^{-3}$ and $L_v = 2.5 \times 10^6$ [J kg⁻¹].

SST [K]	Q_c [W m ⁻²]	Δq_c [g kg ⁻¹]	B [10 ⁻¹⁴ km ⁻¹ s ⁻¹]	A_c [km]
290	86.8	7.31	17.3	5240
295	100	8.64	3.16	12100
300	116	10.5	2.28	13900
305	135	13.4	4.77	9220
310	156	15	5.39	8790

2.6. Summary and Conclusion

In this chapter, we investigate the formation and dependence of the critical domain size of CSA on SST in RCE experiments over a spherical geometry with various domain sizes up to Earth's radius R . We conducted RCE experiments without planetary rotation using a global nonhydrostatic model, NICAM, with various domain sizes and global uniform SST. We used NICAM with a horizontal grid size of about 14 km without cumulus parameterization to calculate deep convection explicitly. We focused on the quasi-equilibrium states and analyzed the dependence of the equilibrium states on domain size and SST.

The simulation results show a single convective region when the domain size is smaller than or equal to $R/4$ and multiple convective regions when the domain size is greater than $R/4$ (Fig. 2.1 and Fig. A2.1). As domain size increases up to $R/4$, the domain-averaged humidity, and the domain-averaged temperature increase. We found that the domain-averaged physical quantities converge to similar values for both $R/1$ and $R/2$. In particular, a moist adiabat at the critical domain size constrains the temperature profile. This convergence was confirmed for all SSTs. For domain sizes of $R/1$ and $R/2$, the global average statistics are almost the same. As domain size increases, the surface wind speed increases as long as a single convective region forms CSA and the surface latent heat flux increases. The radiative cooling in the free troposphere is controlled by the moisture profile, which is limited by the temperature if the relative humidity does not change significantly in these RCE simulations. Because the vertical temperature profile has the warmest profile constrained by moist adiabat and surface temperature (Fig. 2.3a), a critical domain size must exist to limit the increase in the surface wind speed related to latent heat flux (Fig. 2.9b).

Our study found an energy constraint in addition to the momentum balance described in previous studies (Arnold & Putman, 2018; Yang, 2018a). Previous studies argued that boundary layer flow requires a horizontal pressure gradient due to temperature or moisture anomaly in the boundary layer to balance momentum loss through the surface. Arnold and Putman (2018) pointed out that the larger horizontal scale produces a stronger pressure gradient, enhancing the boundary layer wind speed. We incorporate this fact in a simplified form in our study (Eq. 2-6). In addition, our study shows that there is an upper limit to the surface wind speed because the surface latent heat flux must be approximately balanced by the radiative cooling that occurs in the free troposphere if the

surface sensible heat flux is negligible. With regard to the dependence of the horizontal scale on SST, Yang (2018a) suggested that the pressure gradient caused by the virtual effect of water vapor, which depends on SST, is essential to the horizontal scale of CSA. However, the effect of other processes – such as momentum dissipation time scale or diabatic processes – on the dependence of the horizontal scale on SST is unclear. Our study suggests that a change in circulation structure with increasing SST caused by the changes in diabatic heating affects the horizontal scale of CSA.

For the dependence on SST, we found that the critical domain size does not monotonically change with SST (Table 2.1). It is largest at an SST of around 300 K, and smaller at cooler (290 K) and warmer SSTs (305 and 310 K). We defined various indices for convective aggregation to quantify the horizontal scales of the convective region and determine the natural scale of the convective region, which is the horizontal scale of the convective region at the critical domain size. The natural horizontal scale of convection is almost proportional to the critical domain size, although the fractional area of convection changes with SST and domain size.

To further explain the existence of critical domain size, we analyze the FMSE budget (Fig. 2.7). The increase in the convergence term of the FMSE budget as domain size increases is associated with decreasing FMSE export from the convective region, which is consistent with Patrizio and Randall (2019). Thus, there is no increase in FMSE export from the convective region with increasing domain size, as Arnold and Putman (2018) suggested. Patrizio and Randall (2019) hypothesized that the critical domain size occurs where the convective region switches from exporting FMSE to importing FMSE. However, in our simulations, FMSE export from the convective region is always positive. We argue that the dependency of FMSE export is not essential in determining the critical

domain size. We hypothesize that the critical domain size occurs when the convective region becomes close to the warmest moist adiabat, where the SST limits the temperature of the lower layer, and the convective region cannot be further moistened.

We further analyzed the structure of the overturning circulation of the moisture-height space to investigate the dependence of the critical domain size on SST (Fig. 2.10). Water vapor export occurs near the height of the melting level. This level increases monotonically with increasing SST. However, the associated change in the pattern of radiative cooling at the top of the boundary layer in the moisture-height space is not monotonic. This radiative cooling influences the wind speed in the boundary layer and the structure of the overturning circulation in moisture space (Fig. 2.11). As SST becomes cooler or warmer than 300 K, a lower circulation is strengthened, and the surface wind speed becomes stronger near the convective region. These changes are fundamentally caused by the melting level being high enough when SST is higher than 300 K. If the melting level is high enough, the vertical moisture gradient is enhanced in the lower levels, which results in strong radiative cooling at lower levels and higher surface wind speed near the convective region. This surface wind pattern near the convective region enhances the dependence of surface wind speed on domain size and leads to a smaller critical domain size. We found that the pattern of circulation changes to a pattern characterized by stronger surface winds near the convective region when SST increases from 300 K to 305 K. We speculate that such changes in the pattern of circulation depend on the model, although we think that the non-monotonic dependence on SST exists in all numerical models. This SST dependency would be strongly affected by the model's cloud microphysics and radiation schemes. Wing and Cronin (2016) confirmed by changing radiation schemes that the horizontal scale of CSA is modified. However, we emphasize

that the circulation structure in moisture-height space is important. In this study, we show that the structure of the radiative cooling, which is affected by the detrainment height associated with increasing SST, may control the circulation structure and affect the horizontal scale of CSA.

This study clarifies the dependence of the horizontal scale of CSA on SST. The results show a non-monotonic dependence on SST, which is different from the results of previous studies (e.g., Wing & Cronin, 2016; Yang, 2018a). Of course, differences in the numerical models, such as resolution and physical parameterization, may affect the dependence of the critical domain size on SST. We speculate that differences in the domain shape of the models also have an effect. Previous studies used a domain with a channel shape, which may have trapped the dynamic wave structure more quickly than a sphere shape. In addition, the changes in the structure of the effective circulation in moisture space that we point out in the present study may have been smaller in previous studies. We found that this dependency is closely related to the structure of the overturning circulation in moisture space through the increased rate of surface wind speed with increasing domain size. As domain size increases, the dry subsidence region becomes larger, so the horizontal wind from the boundary layer to the convective region increases due to the law of mass conservation. Previous studies have described this feature (e.g., Patrizio & Randall, 2019). An important factor in controlling the increased surface wind speed rate is the change in the detrainment height from the melting level and resulting radiative cooling profiles. The details of responses may depend on cloud microphysics and convective parameterization schemes. Therefore, further studies on the modulation of the horizontal scale, such as investigating the convective parameterization dependence and the response in higher-resolution models, are needed.

A better theoretical understanding of the horizontal scale of self-aggregation is necessary. Yang (2021) recently proposed a simple model for the spatial scale of self-aggregation using a shallow water system. His model expresses spatial scales by gravity wave velocity, damping time scale, and convective density. Convective density is modeled by a small-scale mass sink, which is balanced by the mass source, radiative cooling. The present study shows the effect of the radiative cooling structure on the horizontal scale of the convective region. We speculate that the vertical structure of radiative cooling may control the horizontal scale by affecting the strength of convection. Further study is needed to link the simple model (e.g., Yang, 2021) with CRM simulations. In addition, the horizontal scale of CSA is so large that it includes the gradient of SST and shortwave radiation in the real world. Future work should investigate horizontal scales using experiments with interactive ocean or prescribed SST gradients in such cases.

A. Appendix

The same figures are seen in the main text (Fig. 2.1) but in other SST experiments.

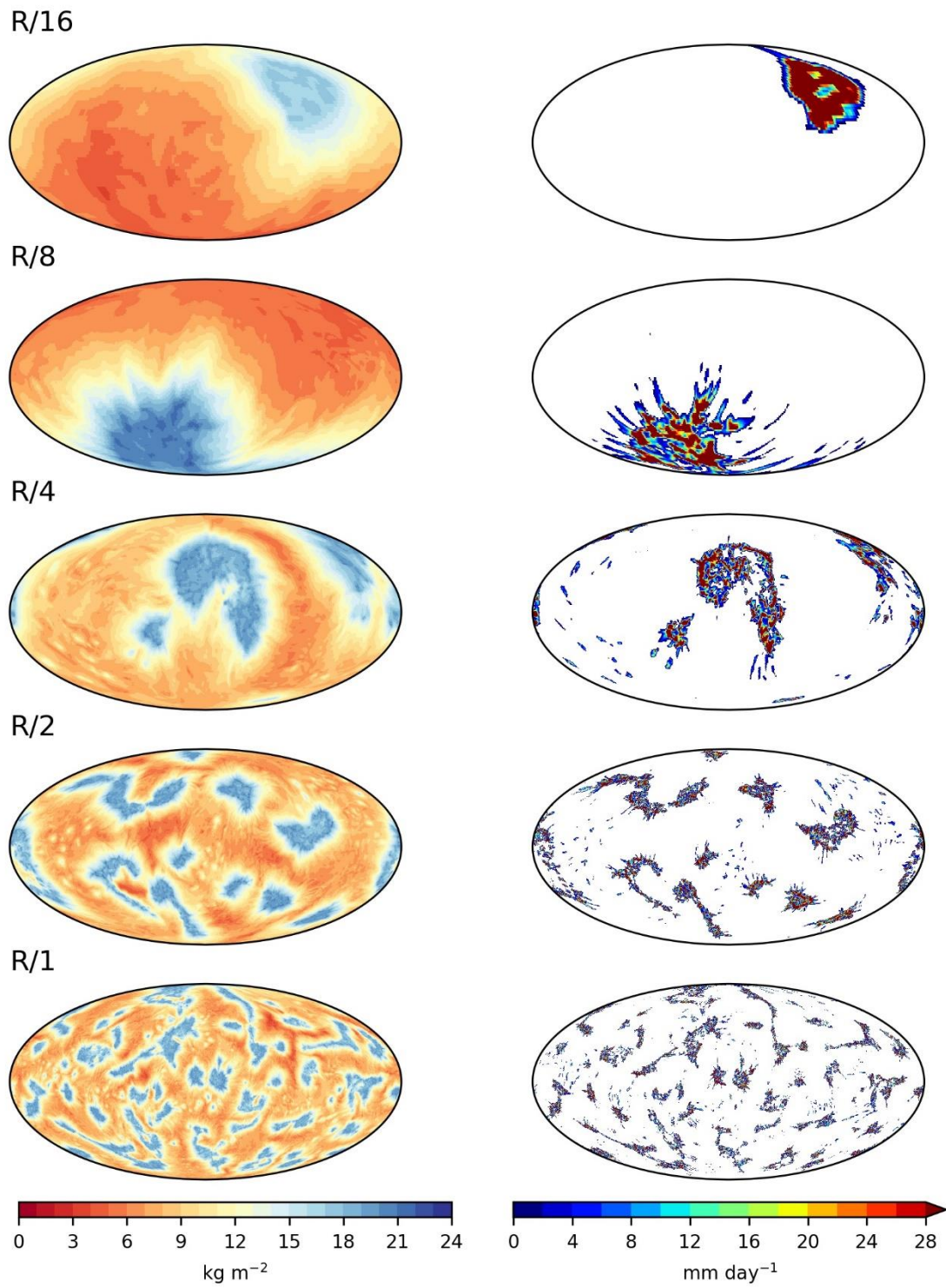


Figure A2.1. Same as Figure 2.1, but for SST290.

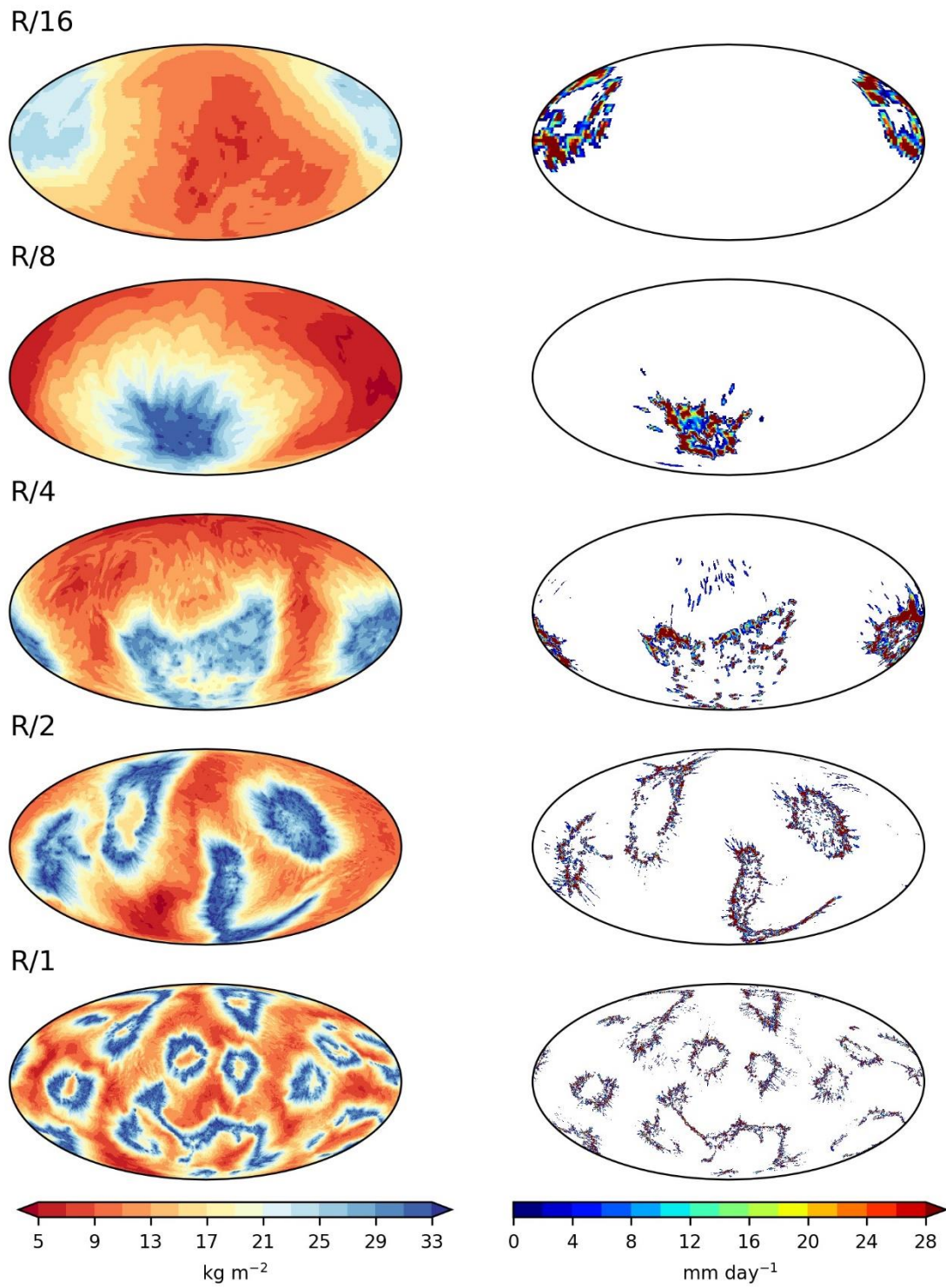


Figure A2.2. Same as Figure 2.1, but for SST295.

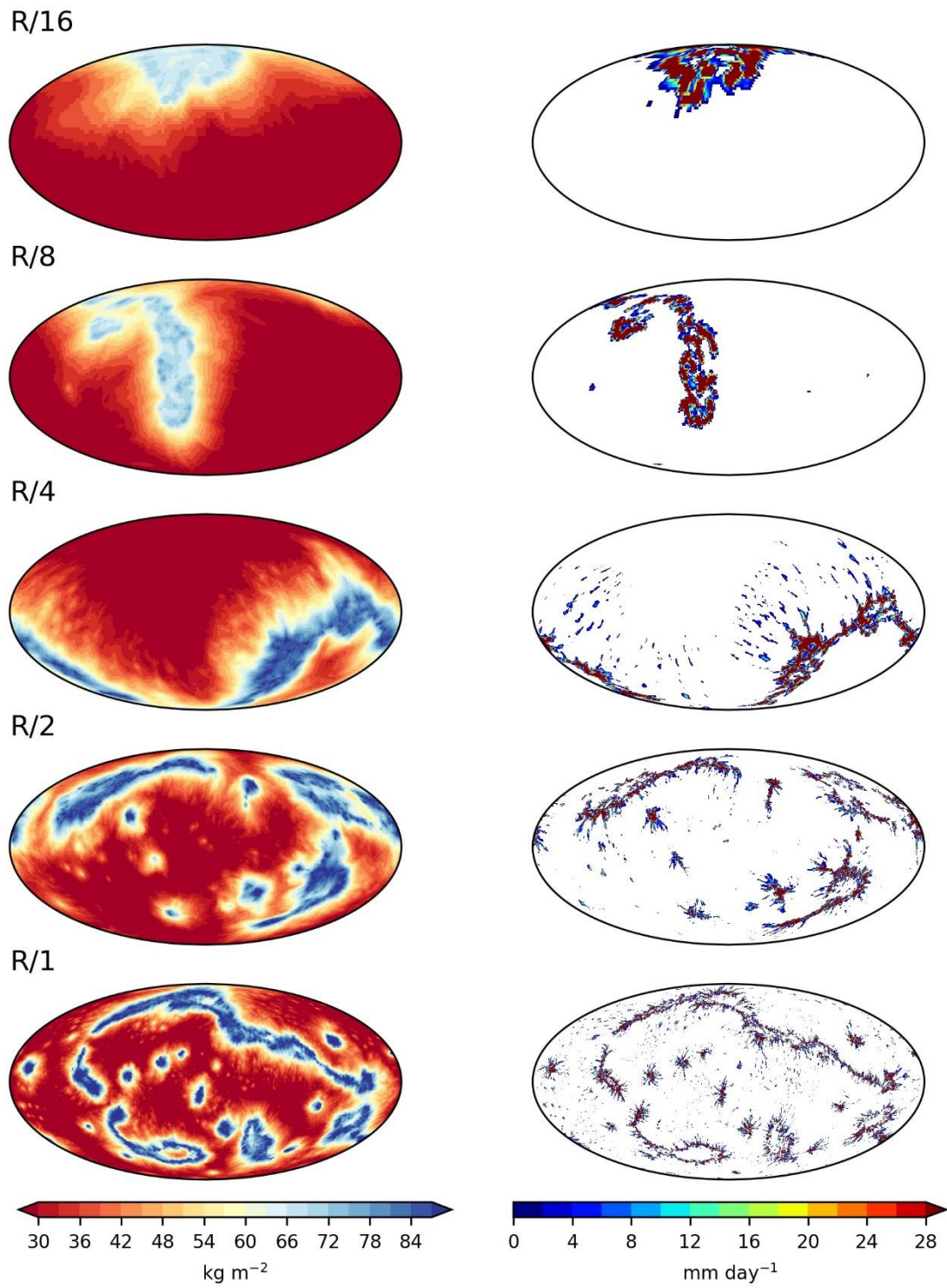


Figure A2.3. Same as Figure 2.1, but for SST305.

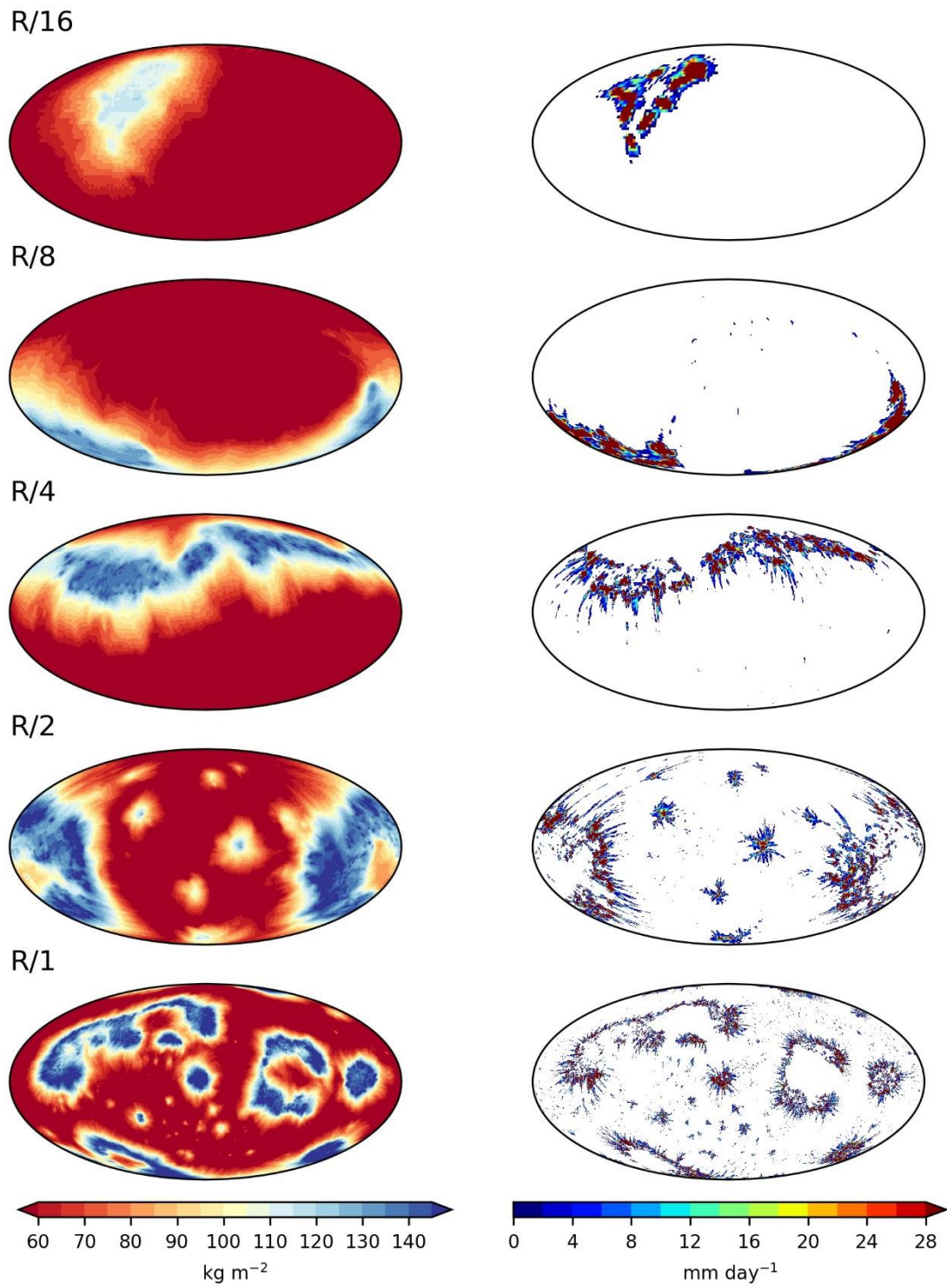


Figure A2.4. Same as Figure 2.1, but for SST310.

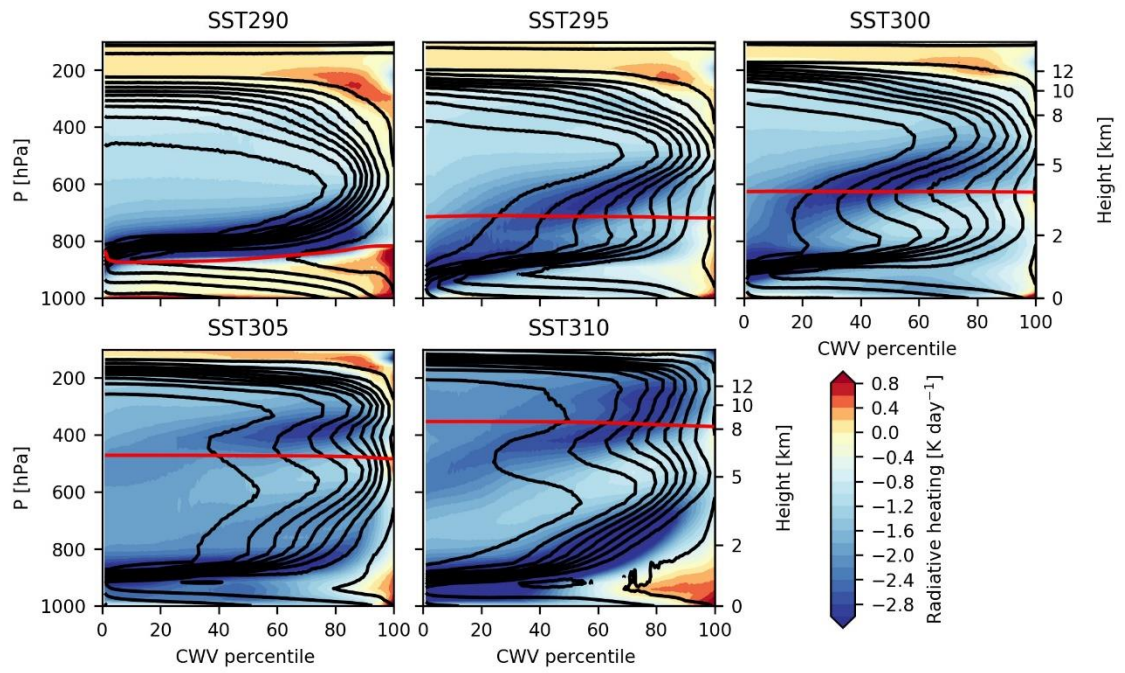


Figure A2.5. Same as Figure 2.10, but the contours show relative humidity (10 % interval).

3. Observational Relationship between the Convective Aggregation, Sea Surface Temperature, and Large-scale circulation

本章については、5年以内に雑誌等で刊行予定のため、非公開。

4. Convective Aggregation in Radiative Convective Equilibrium with Large-scale Forcing

本章については、5年以内に雑誌等で刊行予定のため、非公開。

5. General Conclusions

This dissertation reveals part of the multi-scale response of the cloud and precipitation system to sea surface temperature (SST), which is a fundamental lower boundary condition of the atmosphere. To understand the warming response in our intricate Earth system, we must first understand how the cloud precipitation system changes in increased SST. Although the radiative convection equilibrium (RCE) system is simplistic, it effectively replicates the characteristics of the tropical atmosphere. On the other hand, estimation based on observations is necessary due to the uncertainty of the moist process in numerical models. We analyzed the SST response of convective cloud systems' multiscale aggregation through numerical models and observational data.

In this dissertation, we examine the SST dependence of 1) the maximum horizontal scale of large-scale convective aggregation and 2) the degree of mesoscale aggregation. The first is explored in the context of the maximum horizontal scale of the convective region in large-domain RCE simulation. In contrast, the latter was discussed regarding the change in the degree of aggregation in about 1000 km square domain. This chapter summarizes the main results in Chapters 2, 3, and 4 (Figure 5.1) and describes the relationship among those chapters, the impact of this dissertation, and future perspectives.

5.1. Summary

In Chapter 2, we conduct RCE experiments using a global nonhydrostatic model to investigate the dependence of convective self-aggregation (CSA) on domain size and SST. We use a spherical domain with radii varying from 1 to 1/16 of the Earth's radius and SSTs between 290 and 310 K. A single aggregation occurs at small domain sizes. In contrast, multiple aggregations emerge at sufficiently large domain sizes. Domain-

averaged atmospheric temperature and humidity gradually increase with domain size until they reach convergence in cases of multiple aggregations. As domain size increases, surface wind speed increases and the boundary layer become more humid. Under the constraint of the energy balance, surface evaporation must be limited because the radiative cooling in the free atmosphere is also converged in cases of multiple aggregations. Thus, the convective region shifts from single to multiple aggregations to avoid increasing the surface wind speed. Our results show that the dependence of the horizontal scale of CSA on SST is not monotonic. This dependency is closely related to changes in the structure of the detrainment from the convective region at the melting level, resulting in enhanced radiative cooling at the top of the boundary layer near the convective region for cooler and warmer SSTs. This change in the circulation structure leads to the increased rate of surface wind speed with increasing domain size. This process affects the non-monotonic dependency of the horizontal scale of CSA on SST.

In Chapter 3, our observational analysis seeks to understand the influence of SST and the large-scale circulations, which can be seen as distance to RCE (DRCE), on convective aggregation. We analyze three indices of convective organization: the simple convective aggregation index (SCAI), the index of the organization (Iorg), and the modified subsidence fraction (SF'). SCAI and Iorg show less aggregation as SST increases, while SF' shows more aggregation as SST increases when a simple average is taken. However, SF' does not tend to aggregate as SST increases for the high value of DRCE. SF' does not capture the difference of mean states between aggregation and non-aggregation. Therefore, SF' is an inappropriate index for convective aggregation. When Iorg and SCAI are used as the quantity of convective aggregation, the higher the SST, the less organized; the larger the DRCE, the less organized. In order to clarify the mechanism for the SST

dependence, we examined whether the difference in the mean state between the organized and unorganized condition changes in response to SST. Iorg and SCAI do not show a clear difference in the dependence on SST and DRCE between aggregated and unaggregated mean states. The moist static energy feedback process is unlikely to contribute to the SST dependence of mesoscale aggregation in the real atmosphere, contrary to the previous studies using ideal RCE experiments.

In Chapter 4, we conducted RCE experiments with an external forcing (large-scale forcing; LSF) added to the temperature and water vapor to simulate the equilibrium state with a large-scale upward motion. When the LSF is weak, so-called CSA occurs with a bias of water vapor in the domain. The LSF prevents the occurrence of CSA by introducing moisture to drier regions. As the LSF intensifies, water vapor distribution approaches uniformity, even though convective activity remains aggregated. The same trend as in our observational study existed: the stronger the LSF, the convective system becomes disaggregated, which might be related to an increase in the number of convections. However, the relationship with SST is not solely explicable by the growth in convection numbers. Our results suggest that the weakening of the cold pool associated with SST may influence the decrease in the degree of aggregation.

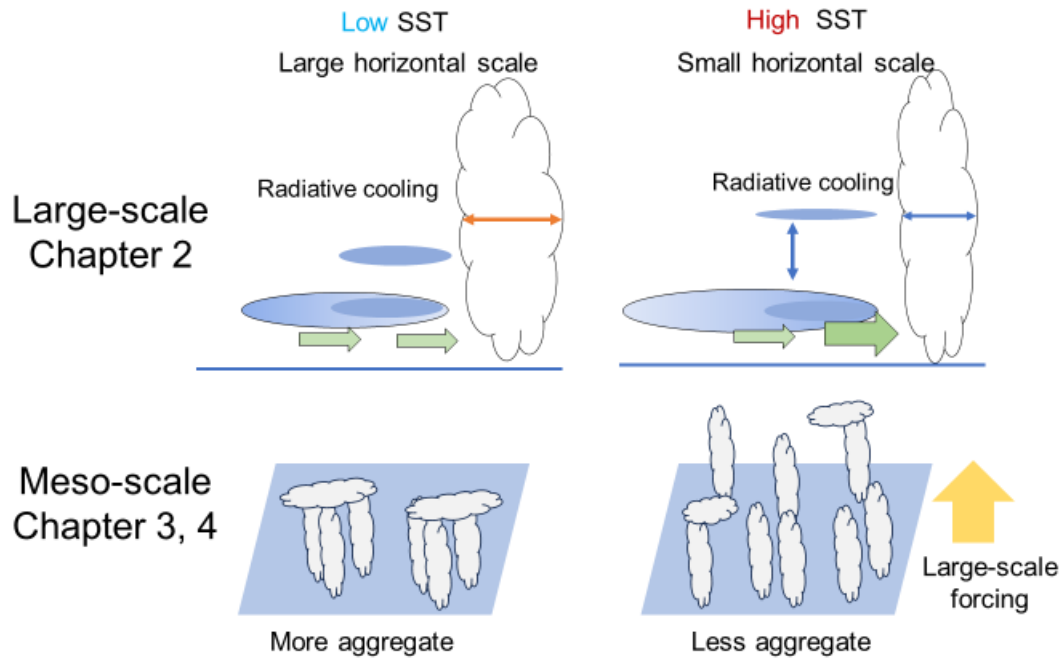


Figure 5.1 A sketch of the summary of this dissertation.

5.2. Concluding discussion

5.2.1. Relationship among chapters

In this thesis, we investigate the dependence of the convective aggregation on SST across two scales: large-scale (global; Chapter 2) and mesoscale (less than 1000 km; Chapters 3 and 4). Chapter 2 delves into the influence of SST on the spatial dimensions of large-scale aggregation. Here, the broadest spatial scale of spontaneously emerging large-scale convective aggregation exceeds 6000 km. The moist convective region corresponds to the region where large-scale upwelling occurs. Naturally, this region is not characterized by a giant single convection. Instead, individual convective cells develop and decline and are maintained within the interior of an upwelling region (Fig. 5.2). The aggregation structure discussed in Chapters 3 and 4 can exist within such a large-scale convective region. Nonetheless, the 14-km mesh grid model deployed in Chapter 2 could

not capture this intricate internal aggregation (see Fig. 5.2). To address this, we analyzed genuine atmospheric conditions and executed idealized experiments using a cloud-resolving model combined with large-scale forcing. This approach allowed us to shed light on the aggregation patterns inherent to vast convective regions.

Chapters 3 and 4 share a strong interrelation. In Chapter 3, we used satellite observation to investigate that aggregation on the 10-degree scale becomes more disaggregate with increasing SST and large-scale forcing (LSF). The results indicate that increasing the number of convections with increasing LSF affects disaggregation. However, large-scale upwelling and SSTs are tightly coupled in the tropical atmosphere, and separating their contributions is difficult. Therefore, in Chapter 4, we performed RCE experiments with external forcing and examined the effects of large-scale forcing in an idealized numerical simulation.

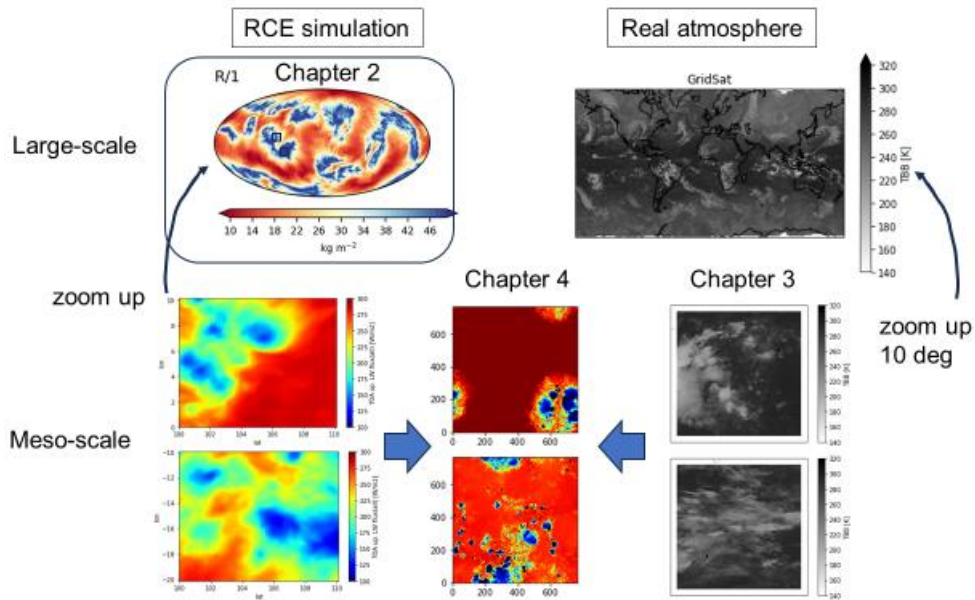


Figure 5.2 A sketch of the relationship among chapters.

5.2.2. Impact of this dissertation

This study reveals the SST dependence of the spatial scale of the aggregation in the RCE experiments. This SST dependence is attributed to the circulation, which is significantly affected by the radiative cooling profile. This is the inaugural study demonstrating the potential correlation between alterations in radiative cooling profiles and spatial scales. Understanding spatial scales of convective activity may offer insights into warming responses associated with large-scale organized convective systems (e.g., MJO). Further studies with other numerical models are expected.

Our findings suggest that mesoscale aggregation becomes weaker with increasing SST. Observational data indicates less aggregate state, attributable to factors linked with SST warming and strong large-scale upwelling forces prevalent in high SST. These findings indicate that mesoscale convective activity may weaken aggregate during global warming. In a previous study, Noda et al. (2019) also pointed out the possibility of weak aggregation as a response to global warming. However, our investigation underscores that their assertion—circulation weakening engenders a less organized state—may be skewed by an inappropriate index. The actual warming response may be determined by the balance between large-scale circulation weakening, which discourages aggregation, and the effects of the increasing SST, which encourages convective aggregation.

The importance of understanding the cold pool process is emphasized in this dissertation. The sensitivity experiments conducted in Chapter 4 show that the cold pool process affects the degree of aggregation in a quasi-equilibrium state. The previous study (e.g., Jeevanjee & Romps, 2013) pointed out the influence of cold pooling in the initiation process of CSA. We point out the importance of the cold pool process affecting convective distribution in the steady state. However, the resolution of our experiments is

too coarse to resolve the cold pool fully. It will be necessary to verify the impact using a higher-resolution model.

5.2.3. Future perspectives

This section outlines future research directions, considering the limitations and open questions stemming from this study.

As mentioned in section 5.2.1, mesoscale aggregation pertains to the coalescence of convective activities within a large-scale aggregation characterized by extensive upwelling. In this dissertation, direct simulations of these phenomena were impossible due to computational cost. Applying large-scale forcing as an external force, as in Chapter 4, can sometimes lead to unnatural solutions (e.g., T305W40 in Chapter 4). Therefore, a high-resolution model that can directly resolve them simultaneously should be used in the future to investigate how the aggregation structure is modulated on SST and environment. Another interesting question is how and to what extent mesoscale aggregated structure influences larger-scale aggregation structure using such a model.

In this study, we define aggregation as a bias in water vapor or a uniform distribution of convective activity (I_{org}), as proposed by previous studies. Various indices (summarized by Jin et al., 2022) have been proposed to quantify the degrees of aggregation by the geometric view. However, a few research examine whether an aggregated convective system equates to an organized precipitation system typified by multiple convection cells, extensive stratiform precipitation, and other characteristics. Future research would benefit from embracing a broader perspective that considers not only geometric distribution but also intrinsic convective attributes to dovetail with existing studies.

In the numerical simulations conducted in this study, a fixed SST was used to investigate the SST dependence. The SST dependence is intended to mimic the global warming response. When convective aggregation occurs, the surface downward shortwave radiation increases due to the expansion of the clear-sky region. With global warming in mind, it is imperative to scrutinize how the spatial and mesoscale organization of convective activities reacts in systems where surface temperatures react with atmospheric energy influxes. The next logical step involves using the slab ocean model. The equilibrium state in these simulations requires experimentation with long integrations. In coupled slab-ocean RCE experiments, we observed oscillatory equilibriums within a few months (Coppin & Bony, 2017). Due to computational costs, studies with high-resolution models have only interacted with SSTs in limited regions (e.g., Hohenegger & Stevens, 2016) or with simulations that look at short-term responses (Huang & Wu, 2022). It will be necessary to consider how the maximum scale of aggregation, as examined in Chapter 2, changes under conditions where the SST varies with the energy balance.

While RCE experiments offer a distilled representation of our intricate natural world, shedding light on various climate and tropical atmosphere facets, these insights can sometimes be skewed by uncertainties inherent in numerical modeling. Continuous refinement of numerical models is essential. This improvement can be achieved through juxtaposing findings with satellite (e.g., Roh et al., 2017) and in-situ observations (e.g., Satoh et al., 2021), as well as through model intercomparisons (e.g., RCEMIP; Wing et al., 2018), as the research progresses.

Acknowledgments

Firstly, I would like to express my sincere gratitude to my advisor, Prof. Masaki Satoh. I would also like to express my gratitude to the members of my dissertation committee, Profs. Tomoki Miyakawa, Tomoki Tozuka, Yukari Takayabu, and Masahiro Watanabe.

I am grateful to my colleague Drs. Daisuke Takasuka, Katsutoshi Fukuzawa, Shoichiro Kido, Yuichi Minamihara, Dai Koshin and Mr. Yuki Takano. I also acknowledge the members and ex-members of the Department of Physical Oceanography in AORI. Prof. Emer. Hiroshi Niino, Prof. Keita Iga, Drs. Junshi Ito, Tomoki Ohno, Woosub Roh, and Eigo Tochimoto gave me constructive questions and suggestions at the regular seminar. I also thank Ms. Hitomi Hibino, Mr.'s Shinichi Kodama, Koryu Yamamoto, Yuta Goto, Kosuke Ikehata, and Hiroshi Morii for their encouragement.

Finally, I would like to sincerely thank my parents and wife, who have deeply understood all my pursuits and supported me with warm encouragement. This dissertation is dedicated to them.

References

- Abbot, D. S., & Abbot, D. S. (2014). Resolved Snowball Earth Clouds. *Journal of Climate*, 27(12), 4391–4402. <https://doi.org/10.1175/JCLI-D-13-00738.1>
- Arnold, N. P., & Putman, W. M. (2018). Nonrotating Convective Self-Aggregation in a Limited Area AGCM. *Journal of Advances in Modeling Earth Systems*, 10(4), 1029–1046. <https://doi.org/10.1002/2017MS001218>
- Arnold, N. P., & Randall, D. A. (2015). Global-scale convective aggregation: Implications for the Madden-Julian Oscillation. *Journal of Advances in Modeling Earth Systems*, 7(4), 1499–1518. <https://doi.org/10.1002/2015MS000498>
- Banzon, V. F., Reynolds, R. W., Stokes, D., & Xue, Y. (2014). A 1/4°-Spatial-resolution daily sea surface temperature climatology based on a blended satellite and in situ analysis. *Journal of Climate*, 27(21), 8221–8228. <https://doi.org/10.1175/JCLI-D-14-00293.1>
- Banzon, V., Smith, T. M., Mike Chin, T., Liu, C., & Hankins, W. (2016). A long-term record of blended satellite and in situ sea-surface temperature for climate monitoring, modeling and environmental studies. *Earth System Science Data*, 8(1), 165–176. <https://doi.org/10.5194/ESSD-8-165-2016>
- Bao, J., & Sherwood, S. C. (2019). The Role of Convective Self-Aggregation in Extreme Instantaneous Versus Daily Precipitation. *Journal of Advances in Modeling Earth Systems*, 11(1), 19–33. <https://doi.org/10.1029/2018MS001503>
- Bao, J., Sherwood, S. C., Colin, M., & Dixit, V. (2017). The Robust Relationship Between Extreme Precipitation and Convective Organization in Idealized Numerical Modeling Simulations. *Journal of Advances in Modeling Earth Systems*. <https://doi.org/10.1002/2017MS001125>

Becker, T., Stevens, B., & Hohenegger, C. (2017). Imprint of the convective parameterization and sea-surface temperature on large-scale convective self-aggregation. *Journal of Advances in Modeling Earth Systems*, 9(2), 1488–1505. <https://doi.org/10.1002/2016MS000865>

Becker, T., & Wing, A. A. (2020). Understanding the Extreme Spread in Climate Sensitivity within the Radiative-Convective Equilibrium Model Intercomparison Project. *Journal of Advances in Modeling Earth Systems*, 12(10), e2020MS002165. <https://doi.org/10.1029/2020MS002165>

Beljaars, A. C. M., & Holtslag, A. A. M. (1991). Flux Parameterization over Land Surfaces for Atmospheric Models. *Journal of Applied Meteorology*, 30(3), 327–341. [https://doi.org/10.1175/1520-0450\(1991\)030<0327:FPOLSF>2.0.CO;2](https://doi.org/10.1175/1520-0450(1991)030<0327:FPOLSF>2.0.CO;2)

Bellon, G., & Coppin, D. (2022). Sensitivity of Convective Self-Aggregation to Subsidence. *Journal of Advances in Modeling Earth Systems*, 14(12), e2021MS002830. <https://doi.org/10.1029/2021MS002830>

Beucler, T., & Cronin, T. (2018). A Budget for the Size of Convective Self-aggregation. *Quarterly Journal of the Royal Meteorological Society*. <https://doi.org/10.1002/qj.3468>

Bony, S., Semie, A., Kramer, R. J., Soden, B., Tompkins, A. M., & Emanuel, K. A. (2020). Observed Modulation of the Tropical Radiation Budget by Deep Convective Organization and Lower-Tropospheric Stability. *AGU Advances*, 1(3). <https://doi.org/10.1029/2019av000155>

Bony, S., Stevens, B., Coppin, D., Becker, T., Reed, K. A., Voigt, A., & Medeiros, B. (2016). Thermodynamic control of anvil cloud amount. *Proceedings of the National Academy of Sciences*, 113(32), 8927–8932. <https://doi.org/10.1073/pnas.1601472113>

Bretherton, C. S., Blossey, P. N., & Khairoutdinov, M. (2005). An energy-balance analysis of deep convective self-aggregation above uniform SST. *Journal of the Atmospheric Sciences*, 62(12), 4273–4292. <https://doi.org/10.1175/JAS3614.1>

Brilouet, P. E., Bouniol, D., Couvreur, F., Ayet, A., Granero-Belinchon, C., Lothon, M., & Mouche, A. (2023). Trade Wind Boundary Layer Turbulence and Shallow Precipitating Convection: New Insights Combining SAR Images, Satellite Brightness Temperature, and Airborne In Situ Measurements. *Geophysical Research Letters*, 50(2), e2022GL102180. <https://doi.org/10.1029/2022GL102180>

Brown, A. R., Derbyshire, S. H., & Mason, P. J. (1994). Large-eddy simulation of stable atmospheric boundary layers with a revised stochastic subgrid model. *Quarterly Journal of the Royal Meteorological Society*, 120(520), 1485–1512. <https://doi.org/10.1002/QJ.49712052004>

Brueck, M., Hohenegger, C., & Stevens, B. (2020). Mesoscale marine tropical precipitation varies independently from the spatial arrangement of its convective cells. *Quarterly Journal of the Royal Meteorological Society*, 146(728), 1391–1402. <https://doi.org/10.1002/qj.3742>

Bryan, G. H. (2021). *The governing equations for CMI*. https://doi.org/10.1142/9789814449717_0001

Bryan, G. H., & Fritsch, J. M. (2002). A benchmark simulation for moist nonhydrostatic numerical models. *Monthly Weather Review*, 130(12), 2917–2928. [https://doi.org/10.1175/1520-0493\(2002\)130<2917:ABSFMN>2.0.CO;2](https://doi.org/10.1175/1520-0493(2002)130<2917:ABSFMN>2.0.CO;2)

Coppin, D., & Bony, S. (2017). Internal variability in a coupled general circulation model in radiative-convective equilibrium. *Geophysical Research Letters*, 44(10), 5142–5149. <https://doi.org/10.1002/2017GL073658>

Coppin, D., & Bony, S. (2015). Physical mechanisms controlling the initiation of convective self-aggregation in a General Circulation Model. *Journal of Advances in Modeling Earth Systems*, 7(4), 2060–2078. <https://doi.org/10.1002/2015MS000571>

Cronin, T. W., & Wing, A. A. (2017). Clouds, Circulation, and Climate Sensitivity in a Radiative-Convective Equilibrium Channel Model. *Journal of Advances in Modeling Earth Systems*, 9(8), 2883–2905. <https://doi.org/10.1002/2017MS001111>

Dai, N., & Soden, B. J. (2020). Convective Aggregation and the Amplification of Tropical Precipitation Extremes. *AGU Advances*, 1(4), e2020AV000201. <https://doi.org/10.1029/2020AV000201>

Daleu, C. L., Plant, R. S., Woolnough, S. J., Sessions, S., Herman, M. J., Sobel, A., et al. (2016). Intercomparison of methods of coupling between convection and large-scale circulation: 2. Comparison over nonuniform surface conditions. *Journal of Advances in Modeling Earth Systems*, 8(1), 387–405. <https://doi.org/10.1002/2015MS000570>

Daleu, C. L., Plant, R. S., Woolnough, S. J., Sessions, S., Herman, M. J., Sobel, A., et al. (2015). Intercomparison of methods of coupling between convection and large-scale circulation: 1. Comparison over uniform surface conditions. *Journal of Advances in Modeling Earth Systems*, 7(4), 1576–1601. <https://doi.org/10.1002/2015MS000468>

Garg, P., Nesbitt, S. W., Lang, T. J., Priftis, G., Chronis, T., Thayer, J. D., & Hence, D. A. (2020). Identifying and Characterizing Tropical Oceanic Mesoscale Cold Pools using Spaceborne Scatterometer Winds. *Journal of Geophysical Research: Atmospheres*, 125(5), e2019JD031812. <https://doi.org/10.1029/2019JD031812>

Grabowski, W. W., & Moncrieff, M. W. (2004). Moisture–convection feedback in the tropics. *Quarterly Journal of the Royal Meteorological Society*, 130(604), 3081–3104. <https://doi.org/10.1256/qj.03.135>

Grabowski, W. W., Moncrieff, M. W., & Kiehl, J. T. (1996). Long-term behaviour of precipitating tropical cloud systems: A numerical study. *Quarterly Journal of the Royal Meteorological Society*, 122(533), 1019–1042. <https://doi.org/10.1002/qj.49712253302>

Graham, N. E., & Barnett, T. P. (1987). Sea Surface Temperature, Surface Wind Divergence, and Convection over Tropical Oceans. *Science*, 238(4827), 657–659. <https://doi.org/10.1126/SCIENCE.238.4827.657>

Haerter, J. O. (2019). Convective self-aggregation as a cold pool driven critical phenomenon. *Geophysical Research Letters*, 2018GL081817. <https://doi.org/10.1029/2018GL081817>

Held, I. M., Hemler, R. S., & Ramaswamy, V. (1993). Radiative-convective equilibrium with explicit two-dimensional moist convection. *Journal of the Atmospheric Sciences*, 50(23), 3909–3927. [https://doi.org/10.1175/1520-0469\(1993\)050<3909:RCEWET>2.0.CO;2](https://doi.org/10.1175/1520-0469(1993)050<3909:RCEWET>2.0.CO;2)

Hersbach, H., Bell, B., Berrisford, P., Hirahara, S., Horányi, A., Muñoz-Sabater, J., et al. (2020). The ERA5 global reanalysis. *Quarterly Journal of the Royal Meteorological Society*, 146(730), 1999–2049. <https://doi.org/10.1002/QJ.3803>

Hersbach, H., Bell, B., Berrisford, P., Hirahara, S., Horányi, A., Muñoz-Sabater, J., et al. (2020). The ERA5 global reanalysis. *Quarterly Journal of the Royal Meteorological Society*, 146(730), 1999–2049. <https://doi.org/10.1002/QJ.3803>

Hohenegger, C., & Jakob, C. (2020). A relationship between ITCZ organization and subtropical humidity. *Geophysical Research Letters*. <https://doi.org/10.1029/2020GL088515>

Hohenegger, C., & Stevens, B. (2016). Coupled radiative convective equilibrium simulations with explicit and parameterized convection. *Journal of Advances in Modeling Earth Systems*, 8(3), 1468–1482. <https://doi.org/10.1002/2016MS000666>

Holloway, C. E., & Woolnough, S. J. (2016). The sensitivity of convective aggregation to diabatic processes in idealized radiative-convective equilibrium simulations. *Journal of Advances in Modeling Earth Systems*, 8(1), 166–195. <https://doi.org/10.1002/2015MS000511>

Holloway, C. E. (2017). Convective aggregation in realistic convective-scale simulations. *Journal of Advances in Modeling Earth Systems*, 9(2), 1450–1472. <https://doi.org/10.1002/2017MS000980>

Holloway, C. E., Wing, A. A., Bony, S., Muller, C., Masunaga, H., L’Ecuyer, T. S., et al. (2017). Observing convective aggregation. *Surveys in Geophysics*, 1–38. <https://doi.org/10.1007/s10712-017-9419-1>

Holloway, C. E., Woolnough, S. J., & Lister, G. M. S. (2013). The effects of explicit versus parameterized convection on the MJO in a large-domain high-resolution tropical case study. Part I: Characterization of large-scale organization and propagation. *Journal of the Atmospheric Sciences*, 70(5), 1342–1369. <https://doi.org/10.1175/JAS-D-12-0227.1>

Houze, R. A. (2004). Mesoscale convective systems. *Reviews of Geophysics*, 42(4), 1–43. <https://doi.org/10.1029/2004RG000150>

Huang, J. De, & Wu, C. M. (2022). A Framework to Evaluate Convective Aggregation: Examples With Different Microphysics Schemes. *Journal of Geophysical Research: Atmospheres*, 127(5), e2021JD035886. <https://doi.org/10.1029/2021JD035886>

Huffman, G. J., Bolvin, D. T., Nelkin, E. J., Wolff, D. B., Adler, R. F., Gu, G., et al. (2007). The TRMM Multisatellite Precipitation Analysis (TMPA): Quasi-Global, Multiyear, Combined-Sensor Precipitation Estimates at Fine Scales. *Journal of Hydrometeorology*, 8(1), 38–55. <https://doi.org/10.1175/JHM560.1>

Islam, S., Bras, R. L., & Emanuel, K. A. (1993). Predictability of mesoscale rainfall in the tropics. *Journal of Applied Meteorology*, 32(2), 297–310. [https://doi.org/10.1175/1520-0450\(1993\)032<0297:POMRIT>2.0.CO;2](https://doi.org/10.1175/1520-0450(1993)032<0297:POMRIT>2.0.CO;2)

Jakob, C., Singh, M. S., & Jungandreas, L. (2019). Radiative Convective Equilibrium and Organized Convection: An Observational Perspective. *Journal of Geophysical Research: Atmospheres*, 124(10), 5418–5430. <https://doi.org/10.1029/2018JD030092>

Jeevanjee, N., & Romps, D. M. (2013). Convective self-aggregation, cold pools, and domain size. *Geophysical Research Letters*, 40(5), 994–998. <https://doi.org/10.1002/grl.50204>

Jin, D., Oreopoulos, L., Lee, D., Tan, J., & Kim, K. Myong. (2022). A New Organization Metric for Synoptic Scale Tropical Convective Aggregation. *Journal of Geophysical Research: Atmospheres*, 127(13), e2022JD036665. <https://doi.org/10.1029/2022JD036665>

Johnson, R. H., Rickenbach, T. M., Rutledge, S. A., Ciesielski, P. E., & Schubert, W. H. (1999). Trimodal characteristics of Tropical convection. [https://doi.org/10.1175/1520-0442\(1999\)012<2397:tcotc>2.0.co;2](https://doi.org/10.1175/1520-0442(1999)012<2397:tcotc>2.0.co;2)

KADOYA, T., & MASUNAGA, H. (2018). New Observational Metrics of Convective Self-Aggregation: Methodology and a Case Study. *Journal of the Meteorological Society of Japan. Ser. II*, 96(6), 535–548. <https://doi.org/10.2151/jmsj.2018-054>

Keith Wilson, D. (2001). An alternative function for the wind and temperature gradients in unstable surface layers. *Boundary-Layer Meteorology*, 99(1), 151–158. <https://doi.org/10.1023/A:1018718707419>

Khairoutdinov, M. F., & Randall, D. A. (2003). Cloud Resolving Modeling of the ARM Summer 1997 IOP: Model Formulation, Results, Uncertainties, and Sensitivities. *Journal of the Atmospheric Sciences*, 60(4), 607–625. [https://doi.org/10.1175/1520-0469\(2003\)060<0607:CRMOTA>2.0.CO;2](https://doi.org/10.1175/1520-0469(2003)060<0607:CRMOTA>2.0.CO;2)

Knapp, K. R., Ansari, S., Bain, C. L., Bourassa, M. A., Dickinson, M. J., Funk, C., et al. (2011). Globally Gridded Satellite Observations for Climate Studies. *Bulletin of the American Meteorological Society*, 92(7), 893–907. <https://doi.org/10.1175/2011BAMS3039.1>

Kuang, Z. (2008). Modeling the Interaction between Cumulus Convection and Linear Gravity Waves Using a Limited-Domain Cloud System–Resolving Model. *Journal of the Atmospheric Sciences*, 65(2), 576–591. <https://doi.org/10.1175/2007JAS2399.1>

Lebsock, M. D., L’Ecuyer, T. S., & Pincus, R. (2017). An Observational View of Relationships Between Moisture Aggregation, Cloud, and Radiative Heating Profiles. *Surveys in Geophysics*, 38(6), 1237–1254. <https://doi.org/10.1007/s10712-017-9443-1>

Louf, V., Jakob, C., Protat, A., Bergemann, M., & Narsey, S. (2019). The Relationship of Cloud Number and Size With Their Large-Scale Environment in Deep Tropical Convection. *Geophysical Research Letters*, 46(15), 9203–9212. <https://doi.org/10.1029/2019GL083964>

Madden, R. A., & Julian, P. R. (1972). Description of global-scale circulation cells in the tropics with a 40–50 day period. *Journal of the Atmospheric Sciences*, 29(6), 1109–1123. [https://doi.org/10.1175/1520-0469\(1972\)029<1109:DOGSCC>2.0.CO;2](https://doi.org/10.1175/1520-0469(1972)029<1109:DOGSCC>2.0.CO;2)

Manabe, S., & Strickler, R. F. (1964). Thermal Equilibrium of the Atmosphere with a Convective Adjustment. *Journal of Atmospheric Sciences*, 21(4), 361–385. [https://doi.org/https://doi.org/10.1175/1520-0469\(1964\)021<0361:TEOTAW>2.0.CO;2](https://doi.org/https://doi.org/10.1175/1520-0469(1964)021<0361:TEOTAW>2.0.CO;2)

Mapes, B. E., & Houze, R. A. (1993). Cloud Clusters and Superclusters over the Oceanic Warm Pool. *Monthly Weather Review*, 121(5), 1398–1416. [https://doi.org/10.1175/1520-0493\(1993\)121<1398:CCASOT>2.0.CO;2](https://doi.org/10.1175/1520-0493(1993)121<1398:CCASOT>2.0.CO;2)

Mapes, B. E., Chung, E. S., Hannah, W. M., Masunaga, H., Wimmers, A. J., & Velden, C. S. (2018). The Meandering Margin of the Meteorological Moist Tropics. *Geophysical Research Letters*, 45(2), 1177–1184. <https://doi.org/10.1002/2017GL076440>

Masunaga, H., Holloway, C. E., Kanamori, H., Bony, S., & Stein, T. H. M. (2020). Transient Aggregation of Convection: Observed Behavior and Underlying Processes. *Journal of Climate*, 34(5), 1685–1700. <https://doi.org/10.1175/jcli-d-19-0933.1>

Masunaga, H., Holloway, C. E., Kanamori, H., Bony, S., & Stein, T. H. M. (2021). Transient aggregation of convection: Observed behavior and underlying processes. *Journal of Climate*, 34(5), 1685–1700. <https://doi.org/10.1175/JCLI-D-19-0933.1>

Masunaga, H., & Mapes, B. E. (2020). A mechanism for the maintenance of sharp tropical margins. *Journal of the Atmospheric Sciences*, 77(4), 1181–1197. <https://doi.org/10.1175/JAS-D-19-0154.1>

Matsugishi, S., & Satoh, M. (2022). Sensitivity of the Horizontal Scale of Convective Self-Aggregation to Sea Surface Temperature in Radiative Convective Equilibrium Experiments Using a Global Nonhydrostatic Model. *Journal of Advances in Modeling Earth Systems*, 14(5), e2021MS002636. <https://doi.org/10.1029/2021MS002636>

Mori, S., Jun-Ichi, H., Tauhid, Y. I., Yamanaka, M. D., Okamoto, N., Murata, F., et al. (2004). Diurnal land-sea rainfall peak migration over Sumatera Island, Indonesian

Maritime Continent, observed by TRMM satellite and intensive rawinsonde soundings. *Monthly Weather Review*, 132(8), 2021–2039. [https://doi.org/10.1175/1520-0493\(2004\)132<2021:DLRPMO>2.0.CO;2](https://doi.org/10.1175/1520-0493(2004)132<2021:DLRPMO>2.0.CO;2)

Muller, C. J., & Held, I. M. (2012). Detailed investigation of the self-aggregation of convection in cloud-resolving simulations. *Journal of the Atmospheric Sciences*, 69(8), 2551–2565. <https://doi.org/10.1175/JAS-D-11-0257.1>

Muller, C., & Bony, S. (2015). What favors convective aggregation and why? *Geophysical Research Letters*, 42(13), 5626–5634. <https://doi.org/10.1002/2015GL064260>

Müller, S. K., & Hohenegger, C. (2020). Self-Aggregation of Convection in Spatially Varying Sea Surface Temperatures. *Journal of Advances in Modeling Earth Systems*, 12(1). <https://doi.org/10.1029/2019MS001698>

Müller, S. K., & Hohenegger, C. (2019). Self-Aggregation of Convection in spatially-varying Sea Surface Temperatures. *Journal of Advances in Modeling Earth Systems*, 2019MS001698. <https://doi.org/10.1029/2019MS001698>

Nakajima, K., & Matsuno, T. (1988). Numerical experiments concerning the origin of cloud clusters in the tropical atmosphere. *Journal of the Meteorological Society of Japan*, 66(2), 309–329. https://doi.org/10.2151/jmsj1965.66.2_309

Nakanishi, M., & Niino, H. (2004). An improved Mellor–Yamada level-3 model with condensation physics: Its design and verification. *Boundary-Layer Meteorology*, 112(1), 1–31. <https://doi.org/10.1023/B:BOUN.0000020164.04146.98>

Nakazawa, T. (1988). Tropical Super Clusters within Intraseasonal Variations over the Western Pacific. *Journal of the Meteorological Society of Japan. Ser. II*, 66(6), 823–839. https://doi.org/10.2151/JMSJ1965.66.6_823

Narasimhan Uma, K., Shankar Das, S., Venkat Ratnam, M., & Viswanathan Suneeth, K. (2021). Assessment of vertical air motion among reanalyses and qualitative comparison with very-high-frequency radar measurements over two tropical stations. *Atmospheric Chemistry and Physics*, 21(3), 2083–2103. <https://doi.org/10.5194/ACP-21-2083-2021>

Narenpitak, P., Bretherton, C. S., & Khairoutdinov, M. F. (2017). Cloud and circulation feedbacks in a near-global aquaplanet cloud-resolving model. *Journal of Advances in Modeling Earth Systems*. <https://doi.org/10.1002/2016MS000872>

Nesbitt, S. W., Zipser, E. J., & Cecil, D. J. (2000). A Census of Precipitation Features in the Tropics Using TRMM: Radar, Ice Scattering, and Lightning Observations. *Journal of Climate*, 13(23), 4087–4106. [https://doi.org/10.1175/1520-0442\(2000\)013<4087:ACOPFI>2.0.CO;2](https://doi.org/10.1175/1520-0442(2000)013<4087:ACOPFI>2.0.CO;2)

Nishizawa, S., Yashiro, H., Sato, Y., Miyamoto, Y., & Tomita, H. (2015). Influence of grid aspect ratio on planetary boundary layer turbulence in large-eddy simulations. *Geoscientific Model Development*, 8(10), 3393–3419. <https://doi.org/10.5194/GMD-8-3393-2015>

Nishizawa, S., Tomita, H., & SCALE, T. (2019). Detailed formulation of SCALE-RM, 131. Retrieved from http://r-ccs-climate.riken.jp/scale/doc/scale_rm_description-5.3.3.pdf

Noda, A. T., Kodama, C., Yamada, Y., Satoh, M., Ogura, T., & Ohno, T. (2019). Responses of Clouds and Large-Scale Circulation to Global Warming Evaluated From Multidecadal Simulations Using a Global Nonhydrostatic Model. *Journal of Advances in Modeling Earth Systems*, 11(9), 2980–2995. <https://doi.org/10.1029/2019MS001658>

Numaguti, A., Okil, R., Nakamura, K., Tsuboki, K., Misawa, N., Asai, T., & Kodama, Y. M. (1995). 4-5-Day-Period Variation and Low-Level Dry Air Observed in the Equatorial Western Pacific during the TOGA-COARE IOP. *Journal of the Meteorological Society of Japan. Ser. II*, 73(2B), 267–290. https://doi.org/10.2151/JMSJ1965.73.2B_267

Ohno, T., & Satoh, M. (2018). Roles of Cloud Microphysics on Cloud Responses to Sea Surface Temperatures in Radiative-Convective Equilibrium Experiments Using a High-Resolution Global Nonhydrostatic Model. *Journal of Advances in Modeling Earth Systems*, 10(8), 1970–1989. <https://doi.org/10.1029/2018MS001386>

Patrizio, C. R., & Randall, D. A. (2019). Sensitivity of Convective Self-Aggregation to Domain Size. *Journal of Advances in Modeling Earth Systems*, 11(7), 1995–2019. <https://doi.org/10.1029/2019MS001672>

Popp, M., & Bony, S. (2019). Stronger zonal convective clustering associated with a wider tropical rain belt. *Nature Communications*, 10(1), 4261. <https://doi.org/10.1038/s41467-019-12167-9>

Posselt, D. J., Van Den Heever, S., Stephens, G., & Igel, M. R. (2012). Changes in the Interaction between Tropical Convection, Radiation, and the Large-Scale Circulation in a Warming Environment. *Journal of Climate*, 25(2), 557–571. <https://doi.org/10.1175/2011JCLI4167.1>

Pscheidt, I., Senf, F., Heinze, R., Deneke, H., Trömel, S., & Hohenegger, C. (2019). How organized is deep convection over Germany? *Quarterly Journal of the Royal Meteorological Society*, 145(723), 2366–2384. <https://doi.org/10.1002/QJ.3552>

Pscheidt, I., Senf, F., Heinze, R., Deneke, H., Trömel, S., & Hohenegger, C. (2019). How organized is deep convection over Germany? *Quarterly Journal of the Royal Meteorological Society*, 145(723), 2366–2384. <https://doi.org/10.1002/QJ.3552>

Raymond, D. J., & Zeng, X. (2005). Modelling tropical atmospheric convection in the context of the weak temperature gradient approximation. *Quarterly Journal of the Royal Meteorological Society*, 131(608), 1301–1320. <https://doi.org/10.1256/QJ.03.97>

Reed, K. A., & Medeiros, B. (2016). A reduced complexity framework to bridge the gap between AGCMs and cloud-resolving models. *Geophysical Research Letters*, 43(2), 860–866. <https://doi.org/10.1002/2015GL066713>

Reed, K. A., Medeiros, B., Bacmeister, J. T., & Lauritzen, P. H. (2015). Global Radiative–Convective Equilibrium in the Community Atmosphere Model, Version 5. *Journal of the Atmospheric Sciences*, 72(5), 2183–2197. <https://doi.org/10.1175/JAS-D-14-0268.1>

Retsch, M. H., Jakob, C., & Singh, M. S. (2020). Assessing Convective Organization in Tropical Radar Observations. *Journal of Geophysical Research: Atmospheres*, 125(7), e2019JD031801. <https://doi.org/10.1029/2019JD031801>

Roh, W., & Satoh, M. (2014). Evaluation of precipitating hydrometeor parameterizations in a single-moment bulk microphysics scheme for deep convective systems over the tropical central pacific. *Journal of the Atmospheric Sciences*, 71(7), 2654–2673. <https://doi.org/10.1175/JAS-D-13-0252.1>

Roh, W., Satoh, M., & Nasuno, T. (2017). Improvement of a cloud microphysics scheme for a global nonhydrostatic model using TRMM and a satellite simulator. *Journal of the Atmospheric Sciences*, 74(1), 167–184. <https://doi.org/10.1175/JAS-D-16-0027.1>

Sato, Y., Nishizawa, S., Yashiro, H., Miyamoto, Y., Kajikawa, Y., & Tomita, H. (2015). Impacts of cloud microphysics on trade wind cumulus: which cloud microphysics processes contribute to the diversity in a large eddy simulation? *Progress in Earth and Planetary Science*, 2(1). <https://doi.org/10.1186/S40645-015-0053-6>

Satoh, M., Matsuno, T., Tomita, H., Miura, H., Nasuno, T., & Iga, S. (2008). Nonhydrostatic icosahedral atmospheric model (NICAM) for global cloud resolving simulations. *Journal of Computational Physics*, 227(7), 3486–3514. <https://doi.org/10.1016/j.jcp.2007.02.006>

Satoh, M. (2014). *Atmospheric circulation dynamics and general circulation models. Atmospheric Circulation Dynamics and General Circulation Models*. Springer Berlin Heidelberg. <https://doi.org/10.1007/978-3-642-13574-3>

Satoh, M., Aramaki, K., & Sawada, M. (2016). Structure of Tropical Convective Systems in Aqua-Planet Experiments: Radiative-Convective Equilibrium Versus the Earth-Like Experiment. *SOLA*, 12(0), 220–224. <https://doi.org/10.2151/sola.2016-044>

Satoh, M., & Hayashi, Y.-Y. (1992). Simple Cumulus Models in One-Dimensional Radiative Convective Equilibrium Problems. *Journal of the Atmospheric Sciences*, 49(14), 1202–1220. [https://doi.org/10.1175/1520-0469\(1992\)049<1202:SCMIOD>2.0.CO;2](https://doi.org/10.1175/1520-0469(1992)049<1202:SCMIOD>2.0.CO;2)

Satoh, M., Stevens, B., Judt, F., Khairoutdinov, M., Lin, S. J., Putman, W. M., & Düben, P. (2019). Global Cloud-Resolving Models. *Current Climate Change Reports* 2019 5:3, 5(3), 172–184. <https://doi.org/10.1007/S40641-019-00131-0>

Satoh, M., Tomita, H., Yashiro, H., Miura, H., Kodama, C., Seiki, T., et al. (2014). The Non-hydrostatic Icosahedral Atmospheric Model: description and development. *Progress in Earth and Planetary Science*, 1(1). <https://doi.org/10.1186/s40645-014-0018-1>

Schneider, T., O’Gorman, P. A., & Levine, X. J. (2010). WATER VAPOR AND THE DYNAMICS OF CLIMATE CHANGES. *Reviews of Geophysics*, 48(3), 3001. <https://doi.org/10.1029/2009RG000302>

Scotti, A., Meneveau, C., & Lilly, D. K. (1998). Generalized Smagorinsky model for anisotropic grids. *Physics of Fluids A: Fluid Dynamics*, 5(9), 2306. <https://doi.org/10.1063/1.858537>

Sekiguchi, M., & Nakajima, T. (2008). A k-distribution-based radiation code and its computational optimization for an atmospheric general circulation model. *Journal of Quantitative Spectroscopy and Radiative Transfer*, 109(17), 2779–2793. <https://doi.org/10.1016/j.jqsrt.2008.07.013>

Semie, A. G., & Bony, S. (2020). Relationship Between Precipitation Extremes and Convective Organization Inferred From Satellite Observations. *Geophysical Research Letters*, 47(9). <https://doi.org/10.1029/2019GL086927>

Sessions, S. L., Herman, M. J., & Sentić, S. (2015). Convective response to changes in the thermodynamic environment in idealized weak temperature gradient simulations. *Journal of Advances in Modeling Earth Systems*, 7(2), 712–738. <https://doi.org/10.1002/2015MS000446>

Sessions, S. L., Sugaya, S., Raymond, D. J., & Sobel, A. H. (2010). Multiple equilibria in a cloud-resolving model using the weak temperature gradient approximation. *Journal of Geophysical Research*, 115(D12), D12110. <https://doi.org/10.1029/2009JD013376>

Silvers, L. G., Stevens, B., Mauritsen, T., & Giorgetta, M. (2016). Radiative convective equilibrium as a framework for studying the interaction between convection and its large-scale environment. *Journal of Advances in Modeling Earth Systems*, 8(3), 1330–1344. <https://doi.org/10.1002/2016MS000629>

Singh, M. S., & Neogi, S. (2022). On the Interaction between Moist Convection and Large-Scale Ascent in the Tropics. *Journal of Climate*, 35(14), 4417–4435. <https://doi.org/10.1175/JCLI-D-21-0717.1>

Sobel, A. H., & Bretherton, C. S. (2000). Modeling tropical precipitation in a single column. *Journal of Climate*, 13(24), 4378–4392. [https://doi.org/10.1175/1520-0442\(2000\)013<4378:MTPIAS>2.0.CO;2](https://doi.org/10.1175/1520-0442(2000)013<4378:MTPIAS>2.0.CO;2)

Stein, T. H. M., Holloway, C. E., Tobin, I., & Bony, S. (2017). Observed relationships between cloud vertical structure and convective aggregation over tropical ocean. *Journal of Climate*, 30(6), 2187–2207. <https://doi.org/10.1175/JCLI-D-16-0125.1>

Stevens, B., Satoh, M., Auger, L., Biercamp, J., Bretherton, C. S., Chen, X., et al. (2019). DYAMOND: the DYNAMICS of the Atmospheric general circulation Modeled On Non-hydrostatic Domains. *Progress in Earth and Planetary Science*, 6(1), 1–17. <https://doi.org/10.1186/S40645-019-0304-Z/FIGURES/9>

Sui, C. H., Lau, K. M., Tao, W. K., & Simpson, J. (1994). The Tropical Water and Energy Cycles in a Cumulus Ensemble Model. Part I: Equilibrium Climate. *Journal of the Atmospheric Sciences*, 51(5), 711–728. [https://doi.org/10.1175/1520-0469\(1994\)051<0711:TTWAEC>2.0.CO;2](https://doi.org/10.1175/1520-0469(1994)051<0711:TTWAEC>2.0.CO;2)

Takayabu, Y. N. (1994). Large-Scale Cloud Disturbances Associated with Equatorial Waves Part I: Spectral Features of the Cloud Disturbances. *Journal of the Meteorological Society of Japan. Ser. II*, 72(3), 433–449. https://doi.org/10.2151/JMSJ1965.72.3_433

Tobin, I., Bony, S., Holloway, C. E., Grandpeix, J.-Y., Sèze, G., Coppin, D., et al. (2013). Does convective aggregation need to be represented in cumulus parameterizations? *J. Adv. Model. Earth Syst*, 5, 692–703. <https://doi.org/10.1002/jame.20047>

Tobin, I., Bony, S., & Roca, R. (2012). Observational evidence for relationships between the degree of aggregation of deep convection, water vapor, surface fluxes, and

radiation. *Journal of Climate*, 25(20), 6885–6904. <https://doi.org/10.1175/JCLI-D-11-00258.1>

Tomita, H. (2008). New microphysical schemes with five and six categories by diagnostic generation of cloud ice. *Journal of the Meteorological Society of Japan*, 86A, 121–142. <https://doi.org/10.2151/jmsj.86A.121>

Tomita, H., & Satoh, M. (2004). A new dynamical framework of nonhydrostatic global model using the icosahedral grid. *Fluid Dynamics Research*, 34(6), 357–400. <https://doi.org/10.1016/J.FLUIDDYN.2004.03.003>

Tompkins, A. M. (2000). The impact of dimensionality on long-term cloud-resolving model simulations. *Monthly Weather Review*, 128(5), 1521–1535. [https://doi.org/10.1175/1520-0493\(2000\)128<1521:TIODOL>2.0.CO;2](https://doi.org/10.1175/1520-0493(2000)128<1521:TIODOL>2.0.CO;2)

Tompkins, A. M. (2001). Organization of tropical convection in low vertical wind shears: The role of cold pools. *Journal of the Atmospheric Sciences*, 58(13), 1650–1672. [https://doi.org/10.1175/1520-0469\(2001\)058<1650:OOTCIL>2.0.CO;2](https://doi.org/10.1175/1520-0469(2001)058<1650:OOTCIL>2.0.CO;2)

Tompkins, A. M., & Craig, G. C. (1998). Radiative–convective equilibrium in a three-dimensional cloud-ensemble model. *Quarterly Journal of the Royal Meteorological Society*, 124(550), 2073–2097. <https://doi.org/10.1002/qj.49712455013>

Tompkins, A. M., & Semie, A. G. (2017). Organization of tropical convection in low vertical wind shears: Role of updraft entrainment. *Journal of Advances in Modeling Earth Systems*, 9(2), 1046–1068. <https://doi.org/10.1002/2016MS000802>

Warren, R. A., Singh, M. S., & Jakob, C. (2020). Simulations of Radiative-Convective-Dynamical Equilibrium. *Journal of Advances in Modeling Earth Systems*, 12(3). <https://doi.org/10.1029/2019MS001734>

Webster, P. J., & Lukas, R. (1992). TOGA COARE: The Coupled Ocean—Atmosphere Response Experiment. *Bulletin of the American Meteorological Society*, 73(9), 1377–1416. [https://doi.org/10.1175/1520-0477\(1992\)073<1377:TCTCOR>2.0.CO;2](https://doi.org/10.1175/1520-0477(1992)073<1377:TCTCOR>2.0.CO;2)

White, B. A., Buchanan, A. M., Birch, C. E., Stier, P., & Pearson, K. J. (2018). Quantifying the effects of horizontal grid length and parameterized convection on the degree of convective organization using a metric of the potential for convective interaction. *Journal of the Atmospheric Sciences*, 75(2), 425–450. <https://doi.org/10.1175/JAS-D-16-0307.1>

Wielicki, B. A., Barkstrom, B. R., Harrison, E. F., Lee, R. B., Smith, G. L., & Cooper, J. E. (1996). Clouds and the Earth’s Radiant Energy System (CERES): An Earth Observing System Experiment. *Bulletin of the American Meteorological Society*, 77(5), 853–868. [https://doi.org/10.1175/1520-0477\(1996\)077](https://doi.org/10.1175/1520-0477(1996)077)

Wing, A. A., & Cronin, T. W. (2016). Self-aggregation of convection in long channel geometry. *Quarterly Journal of the Royal Meteorological Society*, 142(694), 1–15. <https://doi.org/10.1002/qj.2628>

Wing, A. A., & Emanuel, K. A. (2014). Physical mechanisms controlling self-aggregation of convection in idealized numerical modeling simulations. *Journal of Advances in Modeling Earth Systems*, 6(1), 59–74. <https://doi.org/10.1002/2013MS000269>

Wing, A. A., Emanuel, K., Holloway, C. E., & Muller, C. (2017). Convective self-aggregation in numerical simulations: A review. *Surveys in Geophysics*, 1–25. <https://doi.org/10.1007/s10712-017-9408-4>

- Wing, A. A., Reed, K. A., Satoh, M., Stevens, B., Bony, S., & Ohno, T. (2018). Radiative-convective equilibrium model intercomparison project. *Geoscientific Model Development*, 11(2), 793–813. <https://doi.org/10.5194/gmd-11-793-2018>
- Wing, A. A., Stauffer, C. L., Becker, T., Reed, K. A., Ahn, M., Arnold, N. P., et al. (2020). Clouds and Convective Self-Aggregation in a Multimodel Ensemble of Radiative-Convective Equilibrium Simulations. *Journal of Advances in Modeling Earth Systems*, 12(9), e2020MS002138. <https://doi.org/10.1029/2020MS002138>
- Wu, R., Kirtman, B. P., & Pegion, K. (2006). Local Air–Sea Relationship in Observations and Model Simulations. *Journal of Climate*, 19(19), 4914–4932. <https://doi.org/10.1175/JCLI3904.1>
- Wunderling, N., Willeit, M., Donges, J. F., & Winkelmann, R. (2020). Global warming due to loss of large ice masses and Arctic summer sea ice. *Nature Communications*, 11(1). <https://doi.org/10.1038/S41467-020-18934-3>
- Xu, K. M., Hu, Y., & Wong, T. (2019). Convective Aggregation and Indices Examined from CERES Cloud Object Data. *Journal of Geophysical Research: Atmospheres*, 124(24), 13604–13624. <https://doi.org/10.1029/2019JD030816>
- Xu, K.-M., & Arakawa, A. (1992). Semiprognostic Tests of the Arakawa-Schubert Cumulus Parameterization Using Simulated Data. *Journal of Atmospheric Sciences*, 49(24), 2421–2436. [https://doi.org/https://doi.org/10.1175/1520-0469\(1992\)049<2421:STOTAS>2.0.CO;2](https://doi.org/10.1175/1520-0469(1992)049<2421:STOTAS>2.0.CO;2)
- Yanase, T., Nishizawa, S., Miura, H., Takemi, T., & Tomita, H. (2020). New Critical Length for the Onset of Self-Aggregation of Moist Convection. *Geophysical Research Letters*, 47(16), e2020GL088763. <https://doi.org/10.1029/2020GL088763>

Yanase, T., Nishizawa, S., Miura, H., & Tomita, H. (2022). Characteristic Form and Distance in High-Level Hierarchical Structure of Self-Aggregated Clouds in Radiative-Convective Equilibrium. *Geophysical Research Letters*, 49(18), e2022GL100000. <https://doi.org/10.1029/2022GL100000>

Yang, B., & Tan, Z.-M. (2020). The Initiation of Dry Patches in Cloud-Resolving Convective Self-Aggregation Simulations: Boundary Layer Dry-Subsidence Feedback. *Journal of the Atmospheric Sciences*, 77(12), 4129–4141. <https://doi.org/https://doi.org/10.1175/JAS-D-20-0133.1>

Yang, D. (2021). A shallow-water model for convective self-aggregation. *Journal of the Atmospheric Sciences*, 78(2), 571–582. <https://doi.org/10.1175/JAS-D-20-0031.1>

Yang, D. (2019). Convective Heating Leads to Self-Aggregation by Generating Available Potential Energy. *Geophysical Research Letters*, 46(17–18), 10687–10696. <https://doi.org/10.1029/2019GL083805>

Yang, D. (2018). Boundary layer height and buoyancy determine the horizontal scale of convective self-aggregation. *Journal of the Atmospheric Sciences*, 75(2), 469–478. <https://doi.org/10.1175/JAS-D-17-0150.1>

Yang, D. (2018). Boundary Layer Diabatic Processes, the Virtual Effect, and Convective Self-Aggregation. *Journal of Advances in Modeling Earth Systems*, 10(9), 2163–2176. <https://doi.org/10.1029/2017MS001261>

Yasunaga, K., Yoneyama, K., Kubota, H., Okamoto, H., Shimizu, A., Kumagai, H., et al. (2006). Melting Layer Cloud Observed during R/V Mirai Cruise MR01-K05. *Journal of the Atmospheric Sciences*, 63(11), 3020–3032. <https://doi.org/10.1175/JAS3779.1>

YONEYAMA, K. (2003). Moisture Variability over the Tropical Western Pacific Ocean. *Journal of the Meteorological Society of Japan. Ser. II*, 81(2), 317–337.
<https://doi.org/10.2151/jmsj.81.317>

Zhang, C. (1993). Large-Scale Variability of Atmospheric Deep Convection in Relation to Sea Surface Temperature in the Tropics. *Journal of Climate*, 6(10), 1898–1913.
[https://doi.org/10.1175/1520-0442\(1993\)006<1898:LSVOAD>2.0.CO;2](https://doi.org/10.1175/1520-0442(1993)006<1898:LSVOAD>2.0.CO;2)

